fluids

MDPI

Article

A Mixed-Elastohydrodynamic Lubrication Model of a Capped-T-Ring Seal with a Sectioned Multi-Material Film Thickness in Landing Gear Shock Absorber Applications

Aaron Feria Alanis *, Ahmed A. Sheikh Al-Shabab, Antonis F. Antoniadis, Panagiotis Tsoutsanis and Martin Skote

Faculty of Engineering and Applied Sciences, Cranfield University, Cranfield MK43 0AL, UK; a.a.sheikh-al-shabab@cranfield.ac.uk (A.A.S.A.-S.); a.f.antoniadis@cranfield.ac.uk (A.F.A.); panagiotis.tsoutsanis@cranfield.ac.uk (P.T.); m.skote@cranfield.ac.uk (M.S.)
* Correspondence: a.feria-alanis@cranfield.ac.uk

Abstract: Numerical investigations of capped T-ring (CTR) seals performance in reciprocating motion for landing gear shock absorber applications are presented. A lubrication model using the Elastohydrodynamic lubrication theory and deformation mechanics is developed in a multi-material contact zone, and a procedure for coupling fluid and deformation mechanics is introduced. By conducting Finite Element Method (FEM) simulations, the static contact pressure is obtained, which subsequently is used within the model developed herein consisting of a modified Reynolds equation and an asperity contact model, to calculate the fluid film pressure, and the deformation of the fluid channel is determined using an elastic deformation model applied to a multi-component multi-mechanical property channel. These computational results are used for estimations of the seal leakage and friction under various conditions. In addition, the influence of asperity orientation is compared with other parameters, such as sealing pressure and piston velocity. A correlation between asperity orientation and leakage was found, and a general trend of reduced leakage with longitudinally oriented asperities was established.

Keywords: mixed-elastohydrodynamic lubrication; capped T-ring seal; reciprocating seal; landing gears

check for updates

Citation: Feria Alanis, A.; Sheikh Al-Shabab, A.A.; Antoniadis, A.F.; Tsoutsanis, P.; Skote, M. A Mixed-Elastohydrodynamic Lubrication Model of a Capped-T-Ring Seal with a Sectioned Multi-Material Film Thickness in Landing Gear Shock Absorber Applications. *Fluids* **2024**, *9*, 271. https://doi.org/10.3390/fluids9120271

Academic Editor: Chandrashekhar S. Jog

Received: 30 September 2024
Revised: 11 November 2024
Accepted: 13 November 2024
Published: 21 November 2024

Copyright: © 2024 by the authors. Licensee MDPI, Basel, Switzerland. This article is an open access article distributed under the terms and conditions of the Creative Commons Attribution (CC BY) license (https://creativecommons.org/licenses/by/4.0/).

1. Introduction

Sealing systems play an important role in modern-day human life and are widely applied in domestic devices, such as vacuum cleaners, washing machines and food containers. They are also of great importance in heavy industry, including automotive, aerospace, and energy. A drastic example of the significance of sealing systems in the aerospace industry is the tragic destruction of the NASA space shuttle Challenger in 1986, which was attributed to a failure in the sealing performance of elastomeric O-rings [1]. Typical seals are made from elastomer materials which, when subjected to a load, exhibit highly complex, non-linear stress–strain response [1]. Because of the vital role sealing systems have for safety and reliability, it is important to systematically examine the sealing performance under various working conditions. The sealing systems in landing gear applications play a crucial role, especially in shock absorbers. One of the main challenges of sealing systems in shock absorbers is the wide range of working conditions. An example of this is that seals must cope with an aggressive fluid environment at high pressures and temperatures when landing, while still being able to seal in low temperatures experienced at high altitudes [2].

The most widely used elastomer sealing ring profiles in many industry fields are O-rings, due to their simple geometry, applicability over a wide range of pressures and temperatures, and cost-effectiveness [3]. However, O-rings are prone to twist and distort when subjected to high pressures and dynamic motion in applications such as landing gear

shock absorbers [3]. They also tend to extrude between the gaps formed by the sealing clearance, which affects the sealing ring's longevity. To alleviate this problem, substitutions for O-rings have been designed, such as the T-ring, X-ring, L-ring, and D-ring [3]. Over the decades, the usage of T-rings has increased for various applications. However, for research purposes, most of the work published regarding sealing systems is based on O-rings. Only limited findings regarding the performance of T-rings is available. Hydraulic T-rings operate in high pressure conditions, with the possibility of piston motion, outstroke, and instroke, as shown in Figure 1. The successful implementation of a Capped T-ring (CTR) seal prevents leakage of the pressurized oil with minimum friction and avoids the ingress of dust particles from the outside atmospheric conditions.

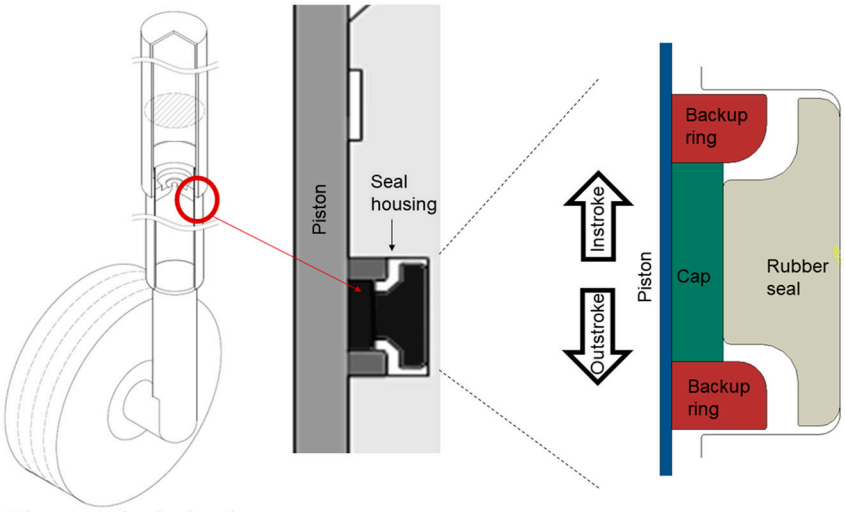


Figure 1. CTR seal and housing cross-sectional geometry, and schematic representation of the T-ring piston sealing system.

According to Nikas [1], sealing system mechanisms are strongly influenced by the contact pressure distribution along the sealing area. Failing to provide appropriate contact between the elements (e.g., O-rings and groove or backup rings, etc.) may lead to leakage. Many studies have performed numerical and experimental analysis of the sealing performance of O-rings. One example is that of Karaszkiewicz [4], who in 1990 developed a model which established the distribution of the contact pressure of an O-ring mounted on a seal groove under different loads. The model was derived based on theoretical assumptions and verified by experiments. In a more recent study, Zhang et al. [5] investigated the effects of precompression, fluid pressure and friction on static and dynamic sealing conditions of O-rings using the Finite Element Method (FEM). They also reported that, in static condition, the friction coefficient has a minimum effect on the O-ring's performance and the Von Mises stresses increase with the fluid pressure. It was also found that pre-compression has great influence on stress distribution. Sukumar et al. [6] developed an experimental procedure and FEM simulations to measure and analyze the sealing performance of O-rings in automotive braking systems. The variation between experimental and numerical simulations did not exceed 4%. The contact pressures obtained from the FEM simulations exceeded the required sealing pressure in actual operating conditions of 3 MPa. The device was further tested up to 5 MPa of sealing pressure, and it was found that leakage may occur when the sealing pressure exceeds 4.7 MPa. In a similar manner, Zhang et al. [7] developed an FEM model to simulate automotive hub bearing O-ring seals using a rigid-flexible combined mechanism and obtained agreement when comparing the contact pressure with experimental analysis. Zho et al. [8,9] investigated the performance of rubber O-rings in high-pressure hydrogen storage applications using FEM simulations. The sealing system consisted of an O-ring rubber and a wedge-ring, which served as a backup to avoid extrusion of the rubber ring. They established that the wedge-ring prevented the O-ring from extruding, and that the

combined seal assembly enhanced the sealing capacity. The sealing performance of O-rings and D-rings in terms of the rubber material hardness was analyzed by Zhang et al. [10]. Other parameters, such as the precompression, medium pressure, and friction coefficient, were studied, along with material hardness ranging from 70 to 90 Shore A hardness. It was found that, in static conditions, the contact pressure of both the D-ring and O-ring increased with the increment of precompression, medium pressure and the hardness of the material. A study of sealing applications oriented to landing gears was performed by Tsala et al. [11], who analyzed the sealing performance of a real piston actuator of a landing gear braking system based on FEM simulations. The numerical results showed that the contact pressure distribution peaks were the largest of all the various sealing pressure values.

The publications mentioned above deal with the sealing system performance only in terms of the contact pressure between tribo-surfaces. However, from a microscopic viewpoint, a fluid film lubricant is formed between the sliding tribo-surfaces, which is essential to reduce damage by friction and wear. The physical properties of the fluid system, such as fluid film thickness, pressure, and lubricant viscosity, can influence the sealing performance. Depending on the lubricating film thickness between two contacting surfaces, the analysis methods may vary. A thick lubricant film can be regarded as hydrodynamic lubrication; however, a reduction in the film thickness can cause the lubrication regime shift to elastohydrodynamic lubrication (EHL). Under this condition, the surface deformation and film thickness are of similar magnitudes. The analysis can be further complicated when the asperities of the surfaces encounter each other, sharing part of the load. This lubrication regime is commonly known as mixed-elastohydrodynamic lubrication (mixed-EHL), which involves the seal material properties.

Early studies in mixed-EHL, EHL, and hydrodynamic lubrication in line contacts were performed by Hess et al. [12]. They performed a series of experiments to analyze the parametric dependence of the friction on the frequency of velocity oscillation, the lubricant viscosity, and the applied normal load. In a more applicable study of sealing systems, Karaszkiewicz [13] showed in experiments that, for an elastomer seal at working condition, a fluid film forms between seal surface and housing. The leakage is determined by the thickness of the fluid film lubricant between the seal and the sealed element. This fluid film generates pressure that may cause leakage if it exceeds the contact pressure. Recently, there has been growing interest in the development of numerical algorithms for mixed-EHL problems. Kumar et al. [14] studied the mixed-EHL condition with directionally oriented roughness for a Rayleigh step bearing and found that transversely oriented asperities generate larger pressures in the contact area. Pei et al. [15] studied the mixed-EHL in line contacts with non-Gaussian rough surfaces. They determined the probability density function (PDF) of rough surface height and asperity height, while the hydrodynamic pressure was obtained by an average flow model and the PDF. Masjedi et al. [16] studied the effect of surface orientation on film thickness, asperity load, and traction coefficient in EHL contacts. It was established that transversely oriented asperities promote larger film thickness compared with isotropic and longitudinal asperities. Furthermore, they found that longitudinal asperities generated the smallest values of film thickness. In terms of EHL applied to O-rings and simple sealing systems, Patri et al. [17] in 1984 studied EHL in elastomeric rectangular seals with rounded edges. They observed that the contact pressure distribution is modified when relative motion exists between the seal and the rod in both the presence and absence of sealed pressure. In more recent studies, Stupkiewicz et al. [18] developed a computational framework to couple the analysis of EHL and the finite deformation theory of elastomeric seals in hydraulic actuators. The hydrodynamic and the finite deformation of the elastomer were successfully coupled by means of FEM. Yuan et al. [19] developed a mixed lubrication model based on the EHL theory to study O-ring seals. The EHL model used by Yuan included asperity contact deformation and was verified with experimental results. Similarly, Han et al. [20] analyzed reciprocating O-ring seals by solving the Reynolds equation coupled with the asperity contact model of Greenwood-Williamson [21] and a deformation model. It was demonstrated in [20] that the oil leakage

and the fluid film thickness increase with the sealing pressure (pressure in the oil part of the system). Thatte et al. [22] studied the EHL contact in a sealing O-ring in transient conditions. In Thatte's work, the change in the rod speed was considered and, similarly to previous publications, the fluid mechanics consist of the solution of the Reynolds equation, while the contact mechanics utilizes the Greenwood–Williamson model. It was shown in [22] that thinner films during the outstroke than during the instroke, and cavitation mainly during the outstroke. are characteristics of non-leaking seals. In a recent study, Zhang et al. [23] presented experimental and theoretical investigations of sealing performance of combined slip rings. They included the temperature change caused by friction in their study, enhancing the EHL analysis by accounting for thermal effects.

The O-ring based research provides a fundamental comprehension of the elastomer sealing system, as observed in the above literature review. The evolved and improved CTR could in general be investigated following a similar approach. However, the FEM and EHL analysis of a CTR seal can become more involved than that of an O-ring due to the complex geometry of the T-ring and the multi-contact zones. This means that, when a lubricant fluid film is formed between tribo-surfaces in a CTR, a multi-material analysis may be involved, which in turn changes the mechanical properties of the fluid film at different sections of the contact zone. In this paper, we investigate the sealing performance of a general CTR seal systems by analyzing the static contact pressure using the ABAQUS FEM software (version 2.7.15), the fluid film pressure by solving the modified Reynolds equation to account for the direction of the asperities, and the asperity contact pressure calculated by the Greenwood–Williamson model. In addition, an elastic deformation model is used in a multi-material contact zone, with different mechanical properties, to account for the fluid film deformation. In Section 2 the methodology is described while the results are presented in Section 3. Conclusions and final comments are reported in Section 4.

2. Methodology

2.1. Materials and Methods

Computation of the static contact pressure in the seal assembly is performed using the commercial software ABAQUS. The multi-component CTR seal is composed by a T-shaped Nitrile Butadiene Rubber (NBR) energizer, a plastic cap, and two polytetrafluorethylene back-up rings, as shown in Figure 2. The basic parameters of the seal assembly are specified in Table 1.

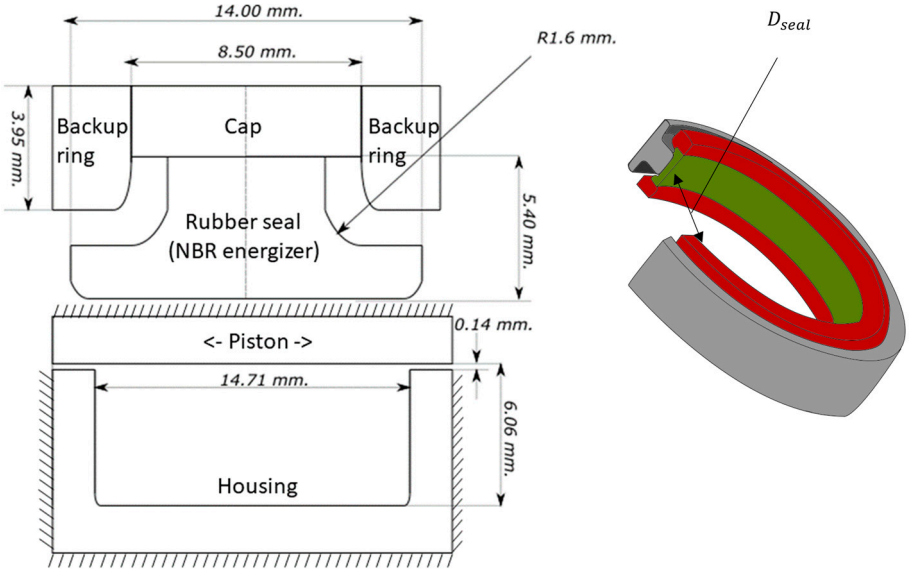


Figure 2. CTR seal and housing cross-sectional schematics, and CTR ring internal diameter.

Table 1. Basic parameters of the sealing assembly.

Basic Parameters	Values	Notation
Seal type	Capped T-shape ring	
Energizer Poisson's ratio	0.499	ν_{NBR}
Cap Poisson's ratio	0.43	ν_C
Backup rings Poisson's ratio	0.46	ν_{BR}
Energizer Mooney-Rivlin (MPa)	1.2517, 0.3129	C_{10}, C_{01}
Cap Young's Modulus (MPa)	802	E_C
Backup rings Young's Modulus (MPa)	500	E_{BR}
Piston Young's Modulus (MPa)	190×10^3	E_p
Piston circumference (m)	0.359	c
Internal diameter of seal (m)	0.1143	D_{seal}
Viscosity-pressure coefficient, (Pa^{-1})	2×10^{-8}	α
Stroke length (m)	0.2	L
Density of oil (kg/m^3)	857.4	ρ_l
Reference viscosity, (Pa·s)	0.0396	η_0
RMS roughness (μm)	0.8	σ
Asperity density (m^{-2})	5×10^{12}	ρ
Asperity radius (μm)	1.5	R

The seal assembly is compressed up to a clearance distance of 0.14 mm between the groove and the piston. The clearance distance and the housing dimensions are selected following the Standard AS4716 specification dash number 460. The compression of the seal in the assembly process is often called precompression, as there will be initial contact pressure between the seal assembly and the housing boundaries when the seal is mounted in the present simulation, due to the elastic properties of the rubber seal. When deformed, the rubber energizer will try to recover its initial shape (elastic recovery), thus pushing the sealing system elements together, exerting a contact pressure between them.

To simplify the numerical simulations, a 2D axisymmetric model is adopted due to the axisymmetric feature of the sealing assembly. Figure 3 shows the finite element boundary conditions. Orange arrows in the figure illustrate displacement boundaries, the arrows in the negative Y direction correspond to the precompression stage, and the ones in the X direction to the instroke–outstroke. Magenta arrows represent the pressure boundary condition applied to the left part of the sealing assembly. The RP stands for the reference point in the groove.

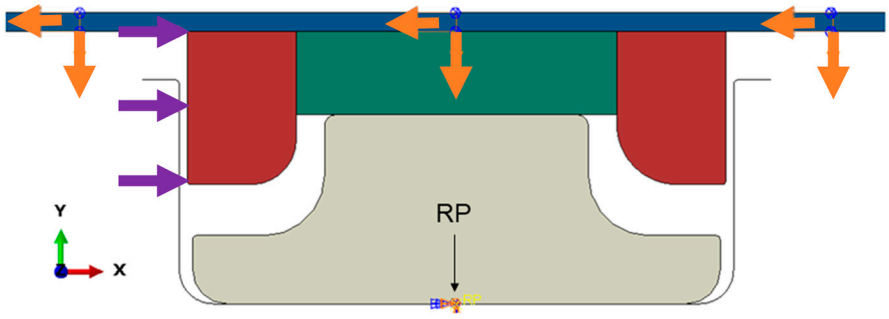


Figure 3. FEM model boundary condition. Orange arrows illustrate displacement boundaries, the precompression in the Y direction and the instroke–outstroke in the X direction. Magenta arrows represent the pressure boundary condition applied to the left part of the sealing assembly. RP stands for reference point in the groove.

To accurately capture the incompressibility behavior of the hyper-elastic material, the rubber ring is meshed with four-node axisymmetric quadrilateral elements with hybrid formulation. The mesh size used in this study is defined in the mesh sensitivity analysis presented in Section 3 of this paper. Ten contact pairs of frictional contact-type are developed in the FEM model simulation. The penalty-based formulation is chosen for all the

contact pairs. The two backup rings and the cap were treated as a single part with sectioned material properties. Each section of the single part was assigned its appropriate material's elastic Young's Modulus and Poisson's ratio.

The FEM simulation and boundary conditions are divided in three steps:

(1) As shown in Figure 3, a displacement boundary condition in the negative Y direction is applied to the top part of the housing until the clearance distance of 0.14 mm is reached. The housing groove is defined as a fixed rigid body with a reference point RP, and the backup rings, cap, and rubber energizer are free to move.

(2) The effect of the sealing pressure is considered in this step. To simulate the seal assembly subjected to a fluid pressure, a pressure boundary condition is applied to the parts of the seal assembly that are in direct contact with the fluid, as presented in Figure 3. The pressure boundary conditions are 5, 10, and 15 MPa, which are selected to simulate high pressures in the oil chamber in a nose landing gear. At this step, the seal assembly backup rings, cap, and rubber seal have free movement in the X and Y directions.

(3) Instroke–Outstroke: a displacement boundary condition is applied to the piston to simulate a reciprocating motion. Instroke corresponds to a displacement in the negative X direction (as is the case in Figure 3), and Outstroke corresponds to a displacement in the positive X-direction.

Modelling elastomers and rubber-like materials is challenging due to their complex mechanical properties. They exhibit incompressibility behavior (Poisson's ratios very close to 0.5, normally larger than 0.49), high deformability, and elastic recovery. The Mooney-Rivlin hyper-elastic model [24,25], is considered an appropriate approach for simulating hyper-elastic rubber-like materials. The two-parameter Mooney-Rivlin model can be expressed as:

$$W = C_{10}(I_1 - 3) + C_{01}(I_2 - 3) \quad (1)$$

where W is the strain energy density, I_1 and I_2 are the first and second strain tensors invariants, respectively, and C_{10} and C_{01} are the Mooney–Rivlin constants that are obtained based on standard engineering stress–strain test of the material at the required temperature. Many research papers estimate these parameters based on experiments performed within their own work [5,8,10]. The data obtained from the stress–strain test is used to calculate the Mooney–Rivlin constants by means of a least-squared function using regression methods, i.e., curve fitting the strain energy density equation into the data from experiments. When uniaxial test data are not available, the Mooney–Rivlin parameters can be estimated using an alternative method, which is based on the elastomer's Youngs Modulus (E) or Shore A hardness (HA). Zhang et al. [7] obtained the Mooney–Rivlin parameters from experimental Shore A hardness tests performed on a nitrile butadiene rubber (NBR) O-ring. According to Zhang, the elastic modulus E can be calculated from the Shore A hardness tests by:

$$E = \frac{15.75 + 2.15HA}{100 - HA} \quad (2)$$

Subsequently, considering the relation between the Mooney–Rivlin coefficients and the elastic modulus, the relations

$$C_{10} = 4C_{01} \quad (3)$$

$$E = 6(C_{10} + C_{01}) \quad (4)$$

were obtained. For the derivation of Equations (2)–(4), see reference [7].

An 80 Shore A hardness is selected to simulate the rubber in a T-ring sealing system yielding Mooney–Rivlin parameters of C_{10} = 1.2517 MPa and C_{01} = 0.3129 MPa. Shore A hardness was selected using the guidelines from Greene Tweed catalogue for a general purpose NBR compound.

2.2. Fluid Mechanics

The fluid film pressure is computed in the contact area between the backup rings, cap, and piston. An example of a channel in the contact area is portrayed in Figure 4 delimited by the dotted yellow line. This channel was selected for analysis because of the sliding motion between the piston, backup rings and the cap. In contrast, the contact between the rubber, backup rings, and the cap experience negligible sliding motion in comparison. A Reynolds equation with flow parameters to account for asperities and cavitation index is used to solve the film thickness and the fluid pressure distribution [19].

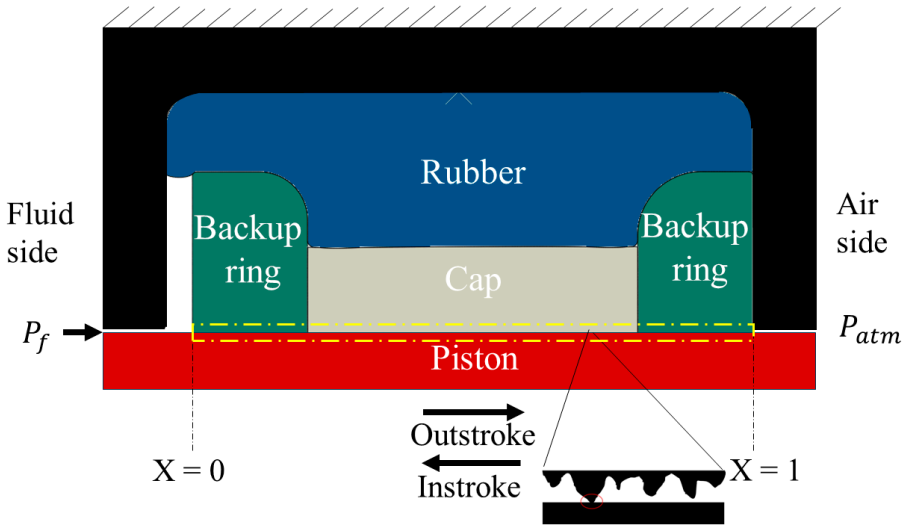


Figure 4. Fluid film channel enclosed by yellow line, and boundary conditions for mixed-EHL solution. Characteristic length for non-dimensional dimension X.

The Reynolds equation is solved using a numerical method suited for partial differential equations by discretizing the physical domain. The central scheme of the finite difference methods is chosen and implemented in a finite number of nodes. The Reynolds equation can be written as:

$$\frac{\partial}{\partial X}\left(\Phi_{xx}\, H^3 \frac{\partial(F\Phi)}{\partial X}\right) = 6\xi \frac{\partial}{\partial X}\{[1+(1-F)\Phi][H_T + \Phi_{scx}]\} \tag{5}$$

In Equation (5), $X = \frac{x}{x_l}$ is the dimensionless coordinate, Φ_{xx} and Φ_{scx} are the pressure flow and shear flow factors, respectively [26,27], and $H = h/\sigma$ is the nondimensional fluid film thickness. The variable F is the cavitation index and Φ is the dimensionless density ($\hat{\rho}$) in the cavitation zone or dimensionless fluid film pressure (P) in the liquid zone. Thus:

$$\begin{cases} \Phi \geq 0,\ F = 1 \text{ and } P = \Phi \text{ (liquid zone)} \\ \Phi < 0,\ F = 0,\ P = 0, \text{ and } \hat{\rho} = 1 + \Phi \text{ (cavitation zone)} \end{cases} \tag{6}$$

where $P = {}^{P_f}/_{P_a}$, with P_f denoting the fluid film pressure and P_a the sealed pressure. The boundary conditions are established as At $X = 0$, $P = 1$, and at $X = 1$, $P = 0$. The term ξ denotes the dimensionless piston speed, $\xi = \frac{\eta_0 U x_l}{(P_{atm}\sigma^2)}$, where U is the piston speed, η_0 is the initial viscosity of the fluid at atmospheric pressure, and x_l is the length of the channel. The viscosity change of the film by the fluid pressure during the numerical iteration is described in Equation (7), where α is the viscosity–pressure coefficient.

$$\eta = \eta_0 e^{\alpha P} \tag{7}$$

H_T is the dimensionless average film thickness, sometimes called the truncated film thickness. Assuming a Gaussian distribution of asperity heights, H_T can be calculated by

$$H_T = \frac{H}{2} + \frac{H}{2} erf\left(\frac{H}{\sqrt{2}}\right) + \frac{1}{\sqrt{2\pi}} e^{\frac{-H^2}{2}} \tag{8}$$

The function *erf* is the error function, which calculates the likelihood of a value within a certain range in a normally distributed dataset.

For $h/\sigma \gg 3$, the roughness effects are not important, and the contact is considered as a smooth surface contact. As $h/\sigma \to 3$, the roughness effects become important [27]. To determine the pressure flow factor, a surface characteristic γ is adopted [27], the value of which is the ratio of the length to the width of the grooves forming the asperities. When $\gamma > 1$, the asperities are elongated in the direction of the flow, while they are elongated in the crossflow direction when $\gamma < 1$. When $\gamma = 1$, the asperities are considered isotropic consisting of circular shapes as shown in Figure 5. In extreme cases when $\gamma = 0$, the asperities are purely transverse while, when $\gamma \to \infty$, the asperities are purely longitudinal. The directional alignment of the asperities depends on the manufacturing process.

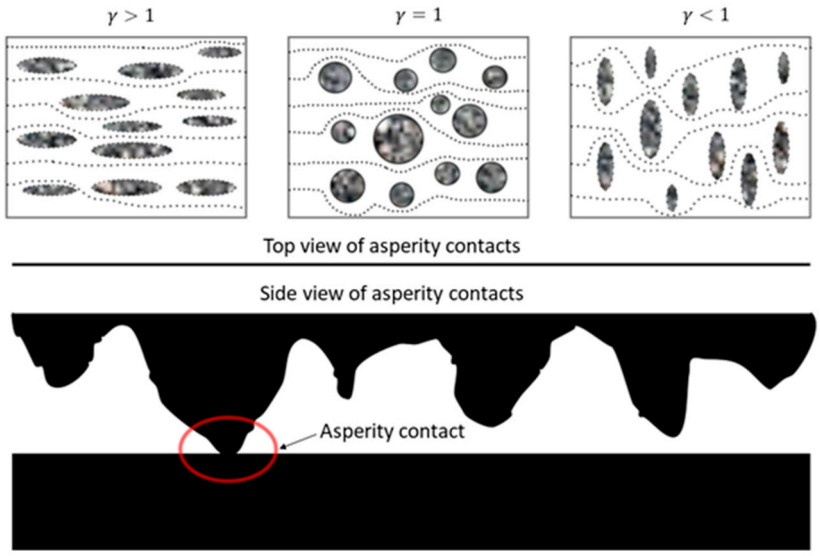


Figure 5. Top view of asperity contact orientations adapted from [27]. Side view of asperity contact between a rough and smooth surface.

To calculate the pressure flow factor, a γ value must be selected and, based on the range of h/σ, appropriate constants D and r from Table 2 must be used [27]. The equations that calculate the pressure flow factor based on γ are

$$\Phi_{xx} = 1 - De^{-rH}, \ \gamma \leq 1 \tag{9}$$

$$\Phi_{xx} = 1 + DH^{-r}, \ \gamma > 1 \tag{10}$$

Table 2. Pressure flow factor constants obtained from [27].

γ	D	r	Range
1/9	1.48	0.42	$h/\sigma > 1$
1/6	1.38	0.42	$h/\sigma > 1$
1/3	1.18	0.42	$h/\sigma > 0.75$
1	0.90	0.56	$h/\sigma > 0.5$
3	0.225	1.5	$h/\sigma > 0.5$
6	0.520	1.5	$h/\sigma > 0.5$
9	0.870	1.5	$h/\sigma > 0.5$

Depending on the roughness configuration of the bearing, Φ_{scx} can be positive, negative or zero. The additional mean flow transport due to the shear flow factor effect is

$$\bar{q}_{xa} = \frac{1}{2} U \sigma \Phi_{scx} \tag{11}$$

Hence, a positive Φ_{scx} means increased flow, and a negative Φ_{scx} means decreased flow. To understand this, assume one surface is rough and the other is smooth. If the rough surface is moving, the fluid carried in the valleys results in an additional flow transport, increasing the mean flow, as revealed by a positive Φ_{scx}. On the other hand, if the smooth surface is moving, then the asperities on the stationary rough surface act as barriers in restricting the flow, hence a negative Φ_{scx}.

To calculate the shear flow factor based on the γ and the ratio h/σ, appropriate shear flow factors are selected from Table 3 [26], and Equations (12) and (13) are solved.

$$\Phi_{scx} = F_1 (h/\sigma)^{a_1} e^{-a_2 (\frac{h}{\sigma}) + a_3 (h/\sigma)^2}, \; h/\sigma \leq 5 \tag{12}$$

$$\Phi_{scx} = F_2 e^{-0.25(\, h/\sigma)} \, , \; h/\sigma > 5 \tag{13}$$

Table 3. Shear flow factor constants obtained from [26].

γ	F_1	a_1	a_2	a_3	F_2
1/9	2.046	1.12	0.78	0.03	1.856
1/6	1.962	1.08	0.77	0.03	1.754
1/3	1.858	1.01	0.76	0.03	1.561
1	1.899	0.98	0.92	0.05	1.126
3	1.560	0.85	1.13	0.08	0.556
6	1.290	0.62	1.09	0.08	0.388
9	1.011	0.54	1.07	0.08	0.295

2.3. Contact Mechanics

Since this study takes place in a mixed-EHL lubrication regime, the asperity contact pressure plays a significant role in the load balance. Thus, an asperity contact model is needed for a comprehensive study of the sealing performance. The Greenwood–Williamson model [21] is widely adopted in mixed-EHL computations. The non-dimensional asperity contact pressure can be expressed as

$$P_c = \frac{4}{3} \frac{1}{(1-\nu^2)} \hat{\sigma}^{1.5} \frac{1}{\sqrt{2\pi}} \int_H^\infty \left(z - H^{1.5} \right) e^{-z^2/2} dz \tag{14}$$

where ν is the poisson's ratio, $\hat{\sigma}$ is the dimensionless root mean squared roughness (RMS), $\hat{\sigma} = \sigma R^{1/3} \rho^{2/3}$, R is the asperity radius, and ρ the asperity density.

2.4. Elastic Deformation

Due to the material properties of the polytetrafluorethylene cap, plastic backup rings and steel piston, which do not present hyper-elastic behavior such as that of the NBR rubber, they are treated as elastic materials. Thus, the elastic deformation of the fluid film is calculated using the Boussinesq equation from Timoshenko's theory of elasticity [28].

The fluid film thickness h_i across the contact area is calculated by

$$h_i = h_0 + \Delta h_i \tag{15}$$

where h_0 is an initial fluid film thickness, and Δh_i is the fluid film deformation at node "i". The fluid film deformation Δh due to a distributed pressure (P_{def}) on the surface is calculated by

$$\Delta h(x,y) = \frac{1-\nu^2}{\pi E}\left[\sum \frac{P_{def_{i,j}} dxdy}{\sqrt{(i-x)^2 dx^2 + (j-y)^2 dy^2}}\right] \tag{16}$$

where E is the elastic Young's modulus, x and y are coordinates in the X and Y directions, ν is the Poisson ratio, the term P_{def} refers to the pressure balance/imbalance, which is the sum of the fluid film pressure P_f from the Reynolds equation and the asperity contact pressure $P_{c_{dim}} = EP_c$ from the Greenwood–Williamson model minus the static contact pressure P_{sc} from the FEM simulations, and the film deformation at any given point is directly proportional to the forces applied at each node. P_{def} is calculated as

$$P_{def} = P_f + P_{c_{dim}} - P_{sc} \tag{17}$$

Due to the one-dimensional (1D) nature of the Reynolds (Equation (5)), the fluid film thickness deformation does not change in the Y-direction in Equation (16). Thus, the nodes of "j" and "y" have always a value of 1, cancelling the $(j-y)^2$ term in Equation (16). This deformation model has been used in relevant studies, such as in the EHL from Peng [29], and Zhou [30]. Similarly, Kumar [14] employs a methodology which considers the pressure balance and the Young's modulus to calculates the fluid film elastic deformation.

Recalling Figure 4, the fluid film is located in the channel formed between the piston, backup rings and cap. This channel involves three different materials with their respective mechanical properties, such as the Young's modulus and Poisson ratios. To address this, the fluid film is discretized in three sections, as shown in Figure 6. The Young's modulus of the piston's stainless steel is several orders of magnitude larger than the cap and backup ring polymers, and its deformation is excluded.

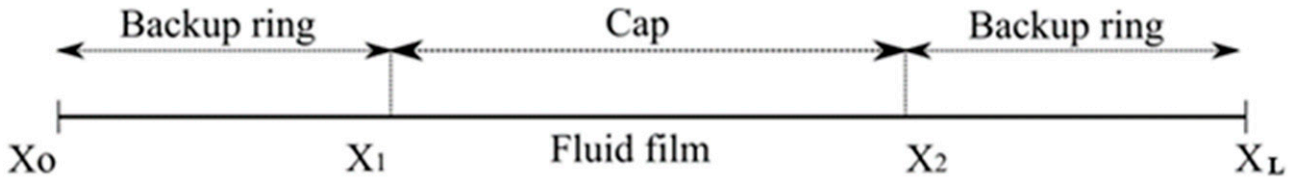


Figure 6. Fluid film channel discretized in 3 sections for different material parameters.

Therefore, the assignment of the Young's modulus and Poisson's ratio in Equation (16) at any x point along the fluid film channel is performed by the following conditions:

$$\begin{cases} E = 500 \text{ MPa},\ \nu = 0.46\ for\ X_o \le X \le X_1 \\ E = 802 \text{ MPa},\ \nu = 0.43\ for\ X_1 < X < X_2 \\ E = 500 \text{ MPa},\ \nu = 0.46\ for\ X_2 \le X \le X_L \end{cases} \tag{18}$$

2.5. Flow Rate and Friction Calculations

The dimensionless flow rate $\hat{q}$ is derived from the Reynolds Equation.

$$\hat{q} = -\Phi_{xx} H^3 \frac{\partial(F\Phi)}{\partial X} + 6\,\xi[1 + (1-F)\Phi](H_T + \Phi_{scx}) \tag{19}$$

The flow rate per unit circumferential length q is

$$q = \frac{P_a \sigma^3 \hat{q}}{12\eta_0 X} \tag{20}$$

The transport fluid volume on a full stroke can be calculated by

$$Q = \frac{L}{U} qc, \tag{21}$$

where L is the length of the stroke, and c is the circumference of the piston. The net flow volume $\overline{Q}$ in a full stroke is the difference between outstroke flow rate Q_{out} and instroke flow rate Q_{ins}, thus, $\overline{Q} = Q_{out} - Q_{ins}$. When the outstroke flow rate is larger than the instroke flow rate, ($Q_{out} > Q_{ins}$) leakage occurs. However, when the instroke flow rate is larger than the outstroke flow rate ($Q_{ins} > Q_{out}$), $\overline{Q}$ is negative, which means that inflow occurs (oil into the sealed space) [13].

In mixed-EHL conditions, the friction is calculated as a combination of Coulomb's friction and viscous friction [19]. Thus, the total friction F_{tot} is expressed as the sum of the Coulomb's friction F_c, and the viscous friction F_v, such as

$$F_v = \pi D_{seal} \int \left(-\frac{\eta U}{h} \left(\varphi_f - \varphi_{fs} \right) + \varphi_{fp} \frac{h}{2} \frac{dP_f}{dx} \right) dx \tag{22}$$

$$F_c = \pi D_{seal} f_c \frac{U}{|U|} \int P_{c_{dim}} dx \tag{23}$$

$$F_{tot} = F_v + F_c \tag{24}$$

The parameters φ_f, φ_{fs}, and φ_{fp} can be found in [26], and f_c is the friction coefficient of 0.05.

2.6. Convergence Criteria and Computational Process

The convergence criteria for the fluid pressure distribution according to the Reynolds equation is

$$\frac{\left| \left(\sum_{i=1}^{n} P_i \right)_{iteration\ k} - \left(\sum_{i=1}^{n} P_i \right)_{iteration\ k-1} \right|}{\left| \left(\sum_{i=1}^{n} P_i \right)_{iteration\ k} \right|} \leq 10^{-4} \tag{25}$$

The convergence criteria for the fluid film deformation is obtained by minimizing the pressure balance P_{def} as:

$$\left(\sum_{i=1}^{n} P_{def_i} \right)_{iteration\ k} - \left(\sum_{i=1}^{n} P_{def_i} \right)_{iteration\ k-1} \leq 0 \tag{26}$$

At every iteration, the pressure balance is reduced until it reaches a minimum value. The computational process of EHL is presented in Figure 7. Firstly, according to the properties of the seal and piston and the operating conditions, the input parameters are defined, then the finite element model is performed to yield the static contact distribution P_{sc}, and the sealing area length. Secondly, an initial film thickness distribution is assumed to solve the Reynolds equation using the MATLAB 9.14 software and the contact pressure using the G–W model. The fluid pressure P_f will not be determined until the convergence criteria is obtained. If the pressure balance is not at its minimum value, the film thickness is updated using the elastic deformation method, and the Reynolds equation and G–W model are solved again. This iterative process ends when the condition in Equation (17) is reached.

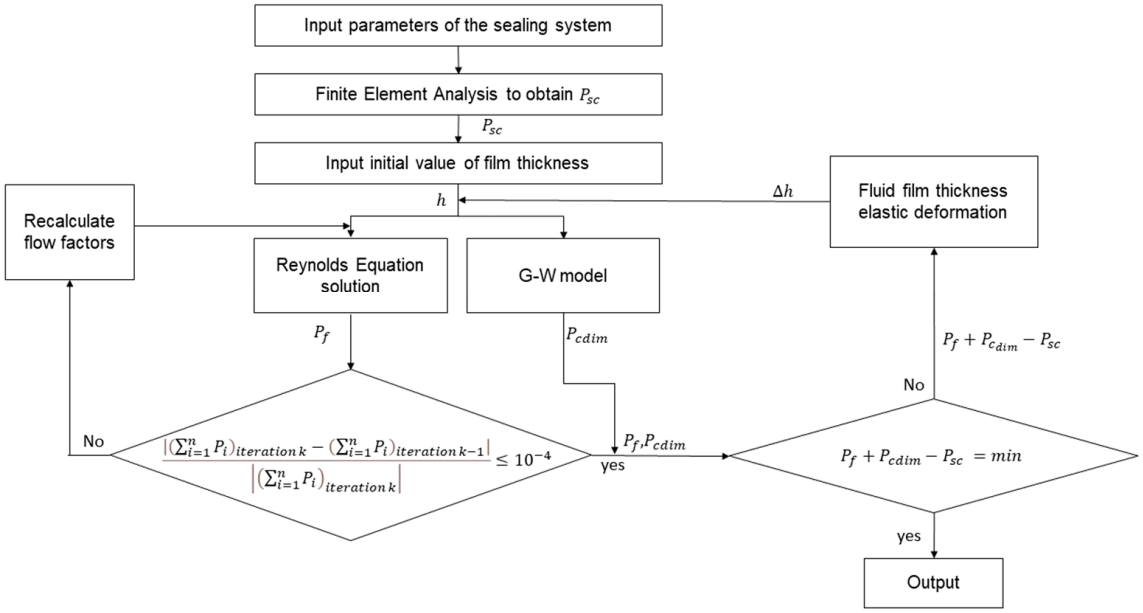


Figure 7. Computational process.

3. Results and Discussion

The contact area in the sealing assembly chosen for investigation is shown in Figure 4, delineated by the dotted yellow line. To analyze the mixed-EHL regime in the channel, the CTR seal assembly was subjected to sealed pressures of 5 MPa, 10 MPa, and 15 MPa in the instroke and outstroke direction with three asperity orientations. To achieve this, a series of FEM simulations are carried out to calculate the static contact pressure between the sealing assembly elements. Subsequently, the static contact pressure obtained through FEM simulations is used as part of the calculations in the mixed-EHL model.

3.1. Static Contact Pressure

Static contact pressure is obtained through FEM simulations using the commercial solver ABAQUS. It is important to verify the implementation of the selected hyper-elastic model, the definition of the contacts between hyper-elastic and elastic materials, as well as the choice of element type and hybrid formulation. Two benchmark cases relevant to sealing systems and hyper-elastic materials were selected for the verification of the FEM model. The two benchmark cases consisted of simulations of O-rings in the precompression stage and originate from two different research groups at Southwest Petroleum University [10] and Henan University of Science and Technology [7]. In benchmark case 1, Zhang et al. [10] performed a series of FEM simulations of O-rings and D-rings at different pre-compression distances (in mm). Benchmark case 2 consist of FEM simulations of O-rings by Zhang et al. [7] validated with experiments. The compression ratio (CR) is defined as the relation between how much the seal is radially compressed when installed in the groove, and the seal's original diameter.

$$CR = \frac{D_0 - D_c}{D_0} \times 100\% \tag{27}$$

where D_0 is the initial elastomer ring diameter, and D_c is the distance between the bottom part of the groove in the seal assembly and the top section of the seal assembly, as shown in Figure 8a.

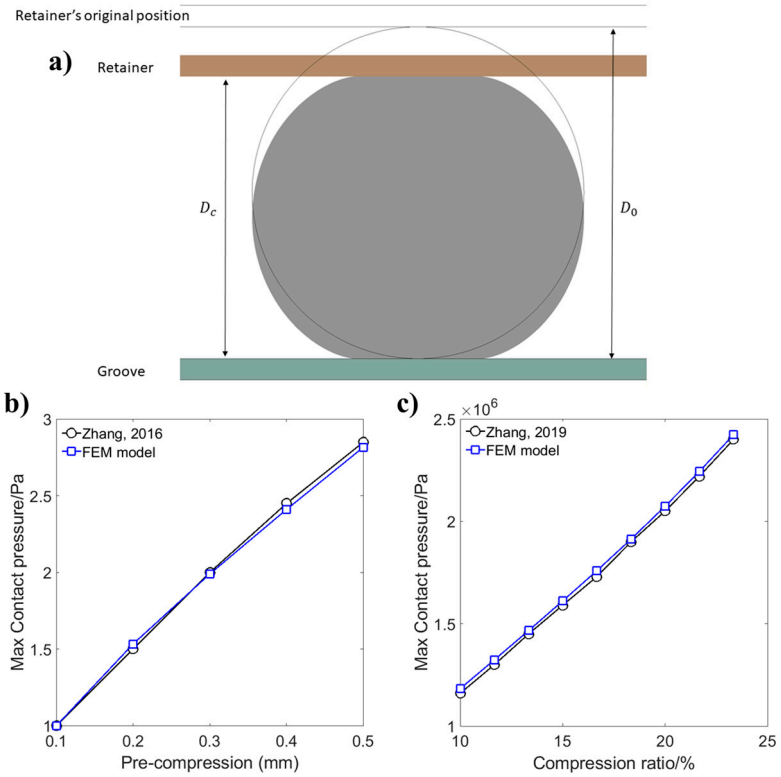


Figure 8. (**a**) Recreated O-ring model. (**b**) Maximum contact pressure at different pre-compressions. A comparison between Zhang et al. [10] and the present FEM model. (**c**) Maximum contact pressure at different compression ratios in comparison with Zhang et al. [7].

A comparison between the maximum contact pressure between the benchmarks and the FEM is presented in Figure 8b,c. In both cases, the maximum contact pressure is in good agreement with the benchmark cases, with only slight differences. This verification study assures that the hyper-elastic model, along with the process used in this work to perform FEM, is capable of accurately simulating hyper-elastic materials, giving confidence in the results presented further in this section, where the CTR is analyzed.

A mesh sensitivity analysis was performed in the area of interest of the CTR assembly. The contact pressure distribution in the junction between the piston, backup rings, and cap, as portrayed in Figure 9a delimited by the yellow line, was examined over a range of different mesh sizes. No significant difference could be observed in the distribution of the contact pressure and the maximum contact pressure along the contact area at different mesh sizes. However, upon a closer look, the mesh size of 0.015 mm exhibits a preferable resolution, especially in contact pressure peaks, compared to coarser meshes, as shown in Figure 9b. Based on this, the mesh size selected for this study is 0.015 mm.

The CTR was simulated under three sealed pressures: 5 MPa, 10 Mpa, and 15 MPa, following the boundary conditions specified in Figure 3. The distributions of the contact pressure between the backup rings, cap and piston are presented in Figure 10. As demonstrated in Figure 10, there are two high contact pressure areas located near the proximity of the cap's edges and a pressure drop in the middle section of the contact area. This can be explained as a by-product of the shape of the elastomeric T-ring, as illustrated in Figures 11 and 12.

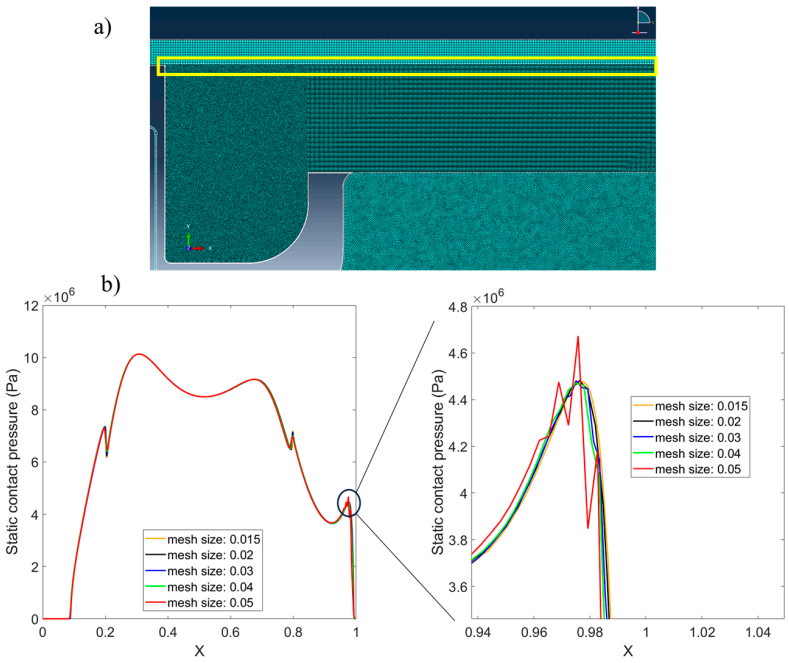


Figure 9. Mesh sensitivity analysis. (**a**) View of the mesh in the contact between the piston, a backup ring and the cap, denoted by yellow line, (**b**) contact pressure between the piston, backup rings and cap at different mesh sizes.

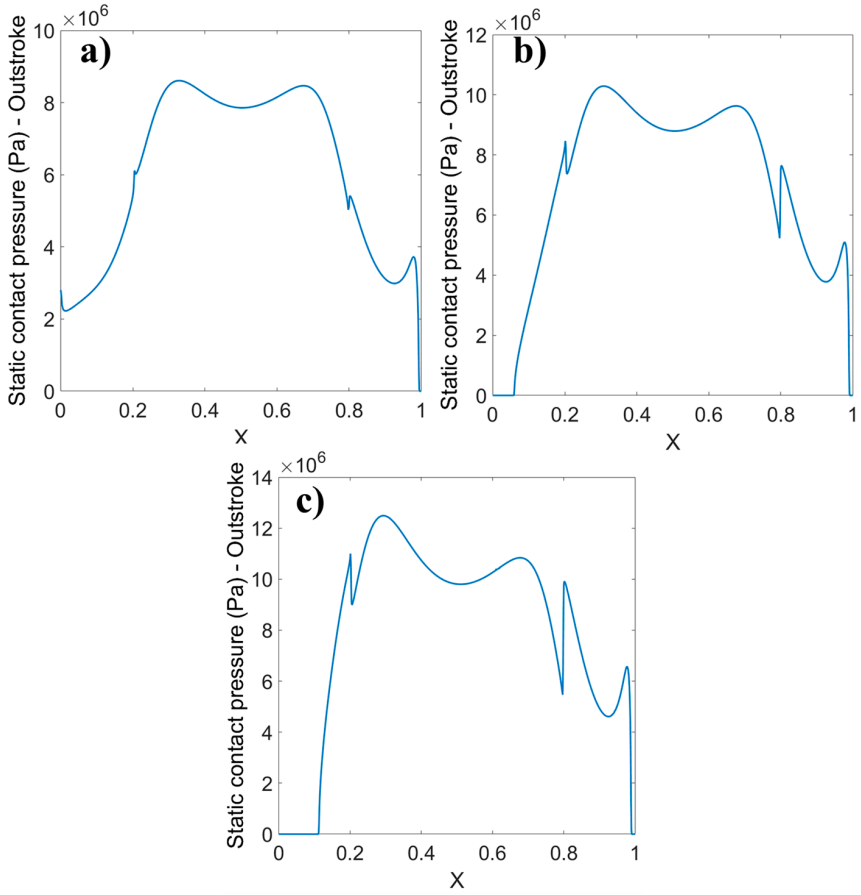


Figure 10. Static contact pressure distribution at sealed pressures of (**a**) 5 MPa, (**b**) 10 MP, (**c**) 15 MPa.

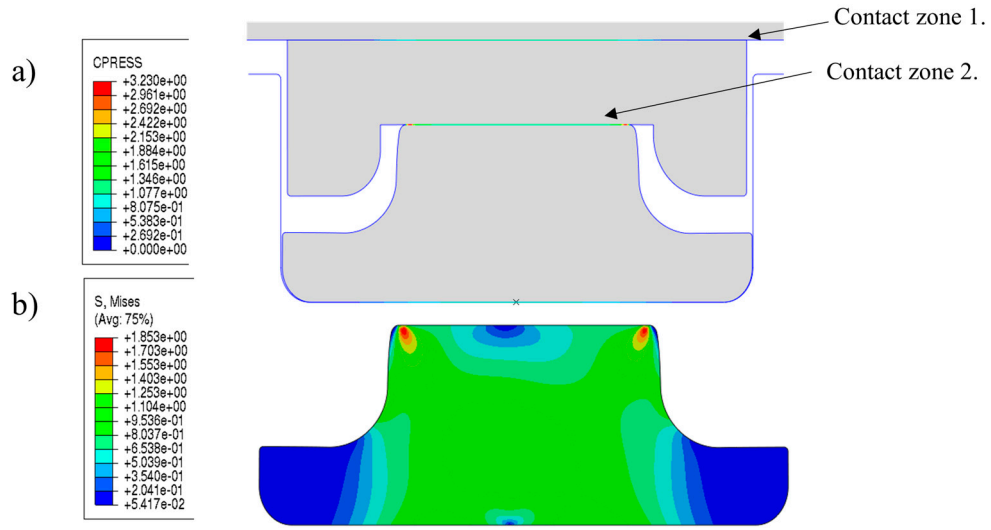


Figure 11. At the initial steps of the precompression stage, (**a**) contact pressure, (**b**) Von Mises stress distribution.

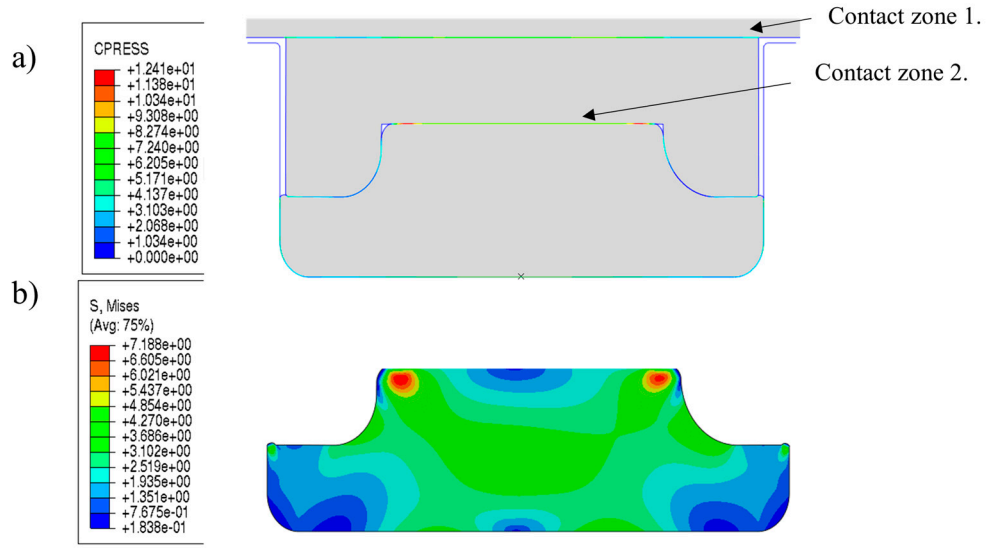


Figure 12. At full precompression, (**a**) contact pressure, (**b**) Von Mises stress distribution.

As the precompression stage initiates (see Figure 3 for boundary conditions), the piston begins to move in the negative Y direction by means of a displacement boundary condition, generating a contact pressure largely between contact zones 1 and 2, as portrayed in Figure 11a. Throughout the precompression stage, contact zones 1 and 2 carry most of the contact pressure loads, and this mainly relates to the inverted T-shape of the elastomeric ring. Initially, only the top side of the elastomeric ring is in contact with the cap, which is moved in the negative Y direction by the piston displacement, squeezing the T ring.

As a result of this initial contact and the shape of the ring, two high contact pressure spots develop in contact zone 2 near the corners of the top side of the T-shape ring, as shown in Figure 11a. Furthermore, at this stage, there are two high peak Von Mises stress concentration spots in the rubber material in the vicinity of the high contact pressure points in contact zone 2, as illustrated in Figure 11b. It can also be observed that, in general, stress distributes mainly in the central area of the rubber T-ring. As the T-shape ring is squeezed until the system is fully pre-compressed as illustrated in Figure 12, high contact pressure peaks in contact zone 2 and the Von Mises stress spots in the rubber increase in size and magnitude. This is because of the elastic recovery property of rubber materials; as the T-ring is compressed, it tends to return to its initial shape, exerting a contact pressure,

which grows with the amount of precompression. When the sealing assembly is fully pre-compressed, as shown in Figure 12b, the contact pressure distribution in contact zone 2 directly influences the contact pressure distribution in contact zone 1. Thus, it is expected to have two high contact pressure areas in contact zone 1 (contact between the cap, backup rings, and piston), in regions similar to the regions of high pressure in contact zone 2, with a drop in pressure in the middle section of the contact area, as demonstrated in Figure 10 for different sealed pressures.

Furthermore, in Figure 10 it is observed that, in most cases, the static contact pressure starts with a value of zero and remains constant in the vicinity of X = 0. However, for the case of 5 MPa of sealed pressure, the static contact pressure at X = 0 is greater than zero and continues increasing across the sealing zone. This difference can be explained in Figure 13 where, for the case of 10 MPa of sealed pressure, a high stress concentration is found in the corners of the part made up of the backup rings and cap, as portrayed in Figure 13a. This high stress concentration suggests that the part is deforming by a bending moment due to the sealed pressure. Based on these results, it can be inferred that the loss of static contact pressure at the beginning of the sealing zone (X = 0) is a by-product of the deformation of the part preventing the contact between the part and the piston in this region, as shown in Figure 13b. These same phenomena occur when the sealed pressure is 15 MPa; however, the deformation is more substantial and thus the region of zero static contact pressure at the beginning of the sealing zone is larger. In contrast, for the case of 5 MPa of sealed pressure, the compounded part is not deformed significantly, and thus there is no loss in the contact with the piston.

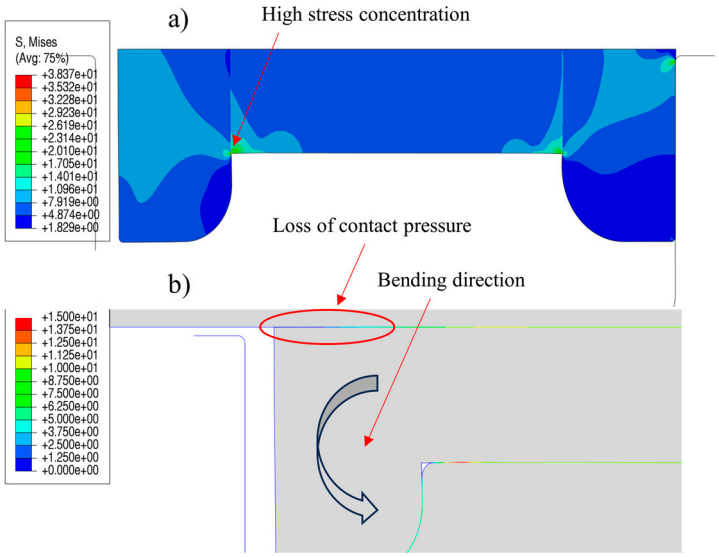


Figure 13. Loss of contact pressure in the vicinity of X = 0 due to part deformation at 10 MPa of sealed pressure. (**a**) Von Mises stress of the part comprising the backup rings and cap, (**b**) static contact pressure.

3.2. Fluid Film Pressure, Asperity Conctact Pressure, and Film Thickness

The CTR assembly was studied in the mixed-EHL regime, with focus on the channel generated in the junction between the piston, backup rings and the cap (contact zone 1 in Figure 12). The methodology employed is illustrated in Figure 7. The input parameters of the sealing system are specified in Table 4 for the three sealed pressures, three piston velocities in the instroke and outstroke directions, and three asperity orientations.

Table 4. Input parameters.

Parameters	Value(s)	
Sealed Pressure	5, 10, 15	MPa
Piston velocity	0.05, 0.1, 0.15	m/s, instroke–outstroke
γ values	1/9, 1, 9	Asperity orientation

It is important to verify the implementation of the mixed-EHL model coupled with the asperity contact model (Equations (5) and (14)), and the deformation method (Equation (16)), as portrayed in Figure 7. As a benchmark case, Yuan et al. [19] developed a partial lubrication model based on the Reynolds equation, and performed a series of numerical simulations of a sealing system comprising an O-ring. In their work, the O-ring was subjected to different sealed pressures and piston velocities. The O-ring assembly model was recreated for this verification case, as shown in Figure 14a, with all the dimensions and the basic parameters given in [19].

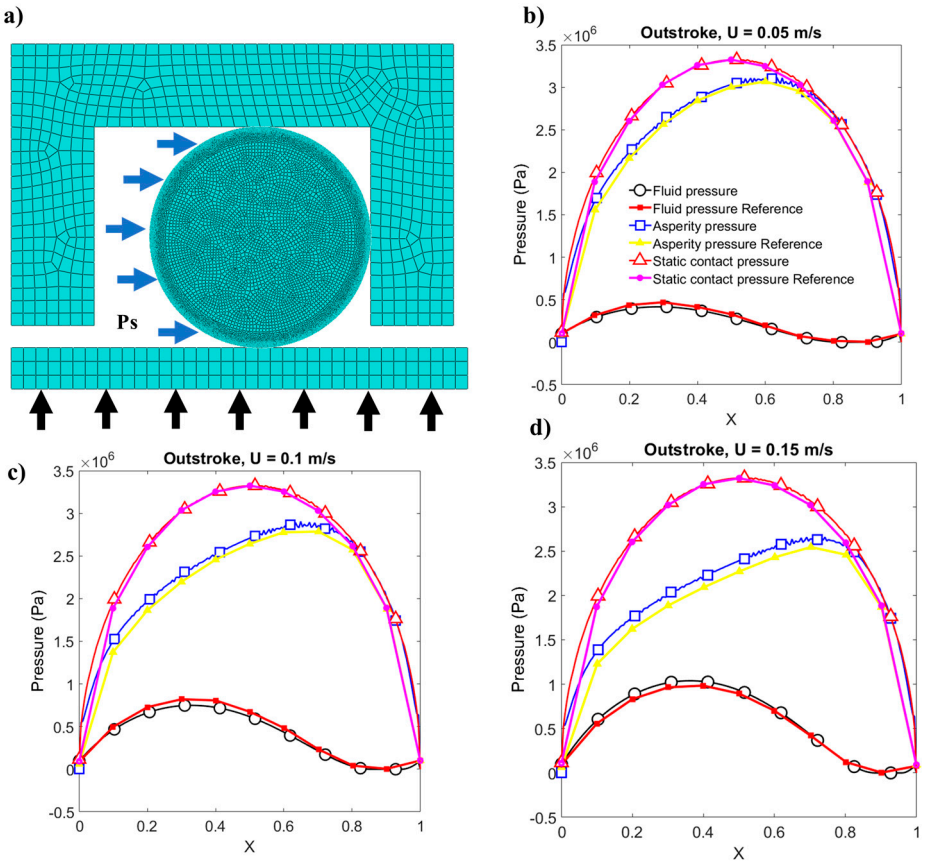


Figure 14. (**a**) Benchmark mesh and boundary conditions of verification case, recreated from [19]. Sealed pressure is 0.1 MPa, (**b**) pressure distributions in the outstroke direction with U = 0.05 m/s, (**c**) pressure distributions in the outstroke direction with U = 0.1 m/s, (**d**) pressure distributions in the outstroke direction with U = 0.15 m/s.

Figure 14 introduces a comparison between the results presented by Yuan et al. [19] and the results obtained from the methodology developed for this paper. The piston velocities for this verification case are 0.05 m/s (b), 0.1 m/s (c), and 0.15 m/s (d), in the outstroke direction. The static contact pressure distribution is obtained from the FEM methodology described in Section 2.1 and is in good agreement with the results obtained in [19] (magenta line in Figure 14). Using static contact pressure distribution, and following the computational process from Figure 7, the fluid film pressure distribution

was obtained solving the Reynolds equation (Equation (5)) iteratively until convergence, and subsequently coupled with the asperity contact G–W model (Equation (14)). The static contact pressure, asperity contact pressure and fluid pressure balance, as shown in Figure 7, are evaluated and then used as input to calculate the fluid channel elastic deformation by means of Equation (16). The process is solved iteratively until the pressure balance converges to a minimum.

Despite the fact that Yuan et al. [19] used the coefficient matrix method to calculate the fluid film deformation, the agreement in fluid film pressure and the asperity contact pressure is excellent (see Figure 14). Furthermore, it was found that the methodology developed in this work predicted cavitation in the contact zones near the air side of the contact, which is in accordance with the results presented in [19]. Overall, this benchmark verification study proved that the methodology described in Figure 7 can produce realistic fluid film pressure and asperity contact pressure results simulating sealing systems.

After the verification of the code for the simpler O-ring, the analysis can now focus on the CTR. Figure 15 presents the fluid film pressure, asperity contact pressure, and the static contact pressure distributions along the channel of the CTR assembly (contact zone 1) at different sealed pressures in the instroke and outstroke conditions with a piston velocity of 50 mm/s. It is important to mention that the number of markers in the figure is for display purposes only and does not represent the amount of data points in these calculations, as the fluid channel was discretized in 955 grid points. The fluid film pressure is larger than the static contact pressure near the oil side of the contact zone, at the beginning of the channel in all cases. This suggests that, in this portion of the channel, the fluid film thickness would be substantially larger than in the rest of the contact zone. The fluid film pressure drops in all cases, reaching the cavitation threshold at a point around 45% of the channel length (0.45 in the nondimensional X axis) for the case of the outstroke direction (in Figure 15a,c,e). From this point, cavitation is encountered in almost the entire of remaining section of the channel in the outstroke motion. In nearly all of the sealing zone, the asperity contact pressure contributes most to balancing the static contact pressure. In the case of the instroke motion (b, d, f), the pressure drop is slightly steeper, especially in the case of 5 MPa of sealed pressure, reaching the cavitation threshold (zero pressure) at a point around 30% of the channel. However, there is a moderate increase in the fluid film pressure near the air side of the sealing zone, before reaching a value of zero, as stated in the boundary conditions for atmospheric pressure, which is more noticeable in the case of 5 MPa of sealed pressure in the instroke motion. Figure 15b can be attributed to an enhanced hydrodynamic effect near the air side, and a similar effect was also reported for slip ring combination seals [23]. Furthermore, similarly in the outstroke direction, the asperity contact pressure contributes the most to the pressure balance in the instroke motion, and cavitation occurs in most of the sealing zone.

From Figure 16, it is observed that higher piston speeds in the outstroke direction promote larger values in the fluid film pressure near the oil side of the channel (X = 0) before reaching the cavitation zone, which is expected, as the fluid pressure is proportional to the dimensionless piston speed, and is attributed to an enhanced hydrodynamic effect with a corresponding decrease in asperity contact pressure. Furthermore, this behavior agrees with the literature [19,23]. On the other hand, in the case of the instroke motion, higher piston speeds produce larger values in the fluid film pressure near the air side of the sealing zone (X = 1). The fluid film pressure distribution in the instroke motion starts decreasing gradually from the oil side until the middle section of the channel, where it reaches cavitation, followed by a subsequent increase. This is more pronounced in the case of 150 mm/s of piston speed.

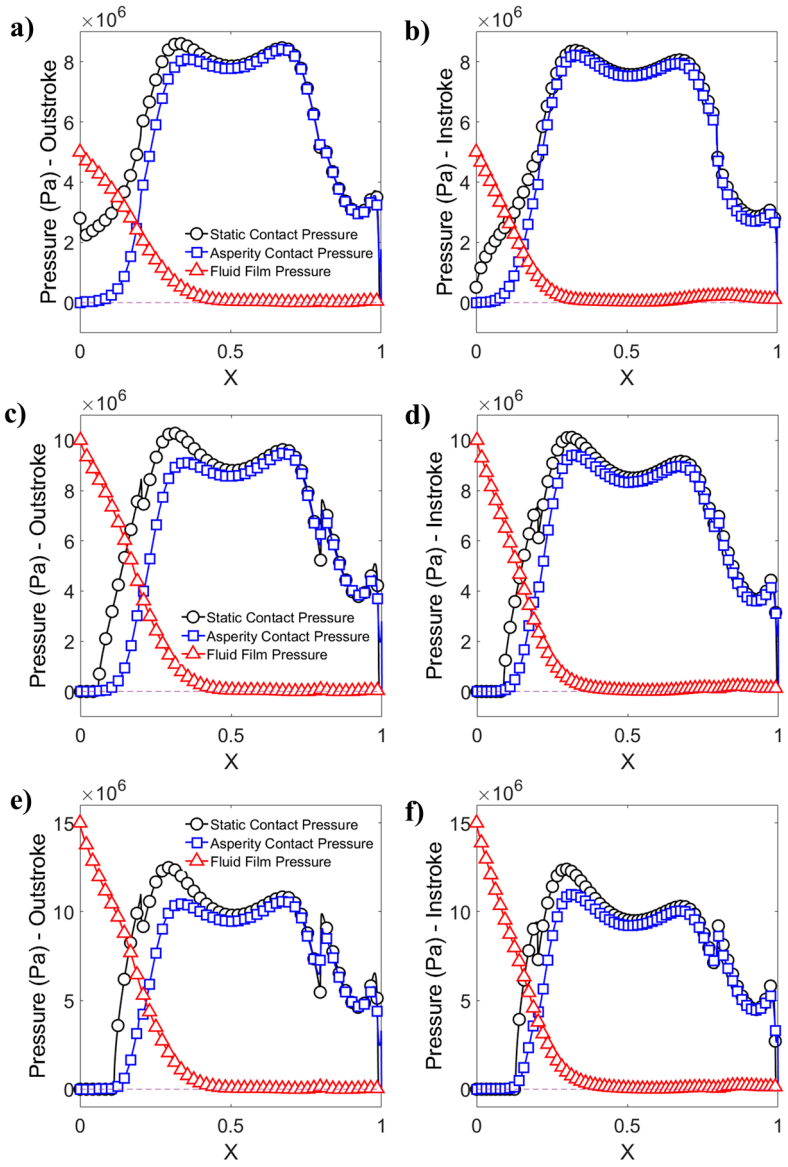


Figure 15. Pressure distributions at different sealed pressures in the instroke and outstroke directions: (**a**,**b**) 5 MPa, (**c**,**d**) 10 MPa, (**e**,**f**) 15 MPa.

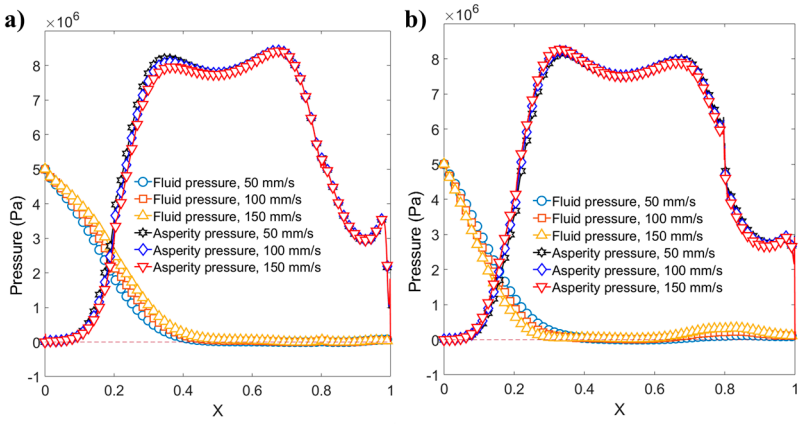


Figure 16. Fluid film pressure and asperity contact pressure distributions at different piston speeds at 5 MPa of sealed pressure: (**a**) Outstroke, (**b**) Instroke.

This phenomenon in the instroke motion can be attributed to an improved hydrodynamic effect near the air side of the sealing zone, and is in good agreement with previous studies on slip ring combination seals [23]. However, this increase in fluid pressure with piston velocity in the instroke direction is less significant compared to the increase in pressure in the outstroke direction. Furthermore, in the instroke motion, there seems to be a negative effect on the fluid pressure with the piston velocity near the oil side of the channel (X = 0). With increasing piston speed, the decrease in fluid pressure from the oil side becomes more pronounced, an effect that has also been reported for slip ring seals [23].

Figure 17 presents the fluid film thickness along the channel at different sealed pressures and piston velocities, in the instroke and outstroke motion. It is evident that, near the oil side of the contact zone (X = 0), the film thickness is at its maximum, which corresponds to the area of the channel where the fluid film pressure is bigger than the static contact pressure at the beginning of the contact zone, as mentioned before. Then, the thickness drops continuously until a point at about 20% of the channel, where it stays relatively constant at a value of around 2 µm. In addition, from these results, it can be noted that the film thickness does not vary much with the piston velocity for this range of pressures and velocities, which agrees with the literature on O-rings [19].

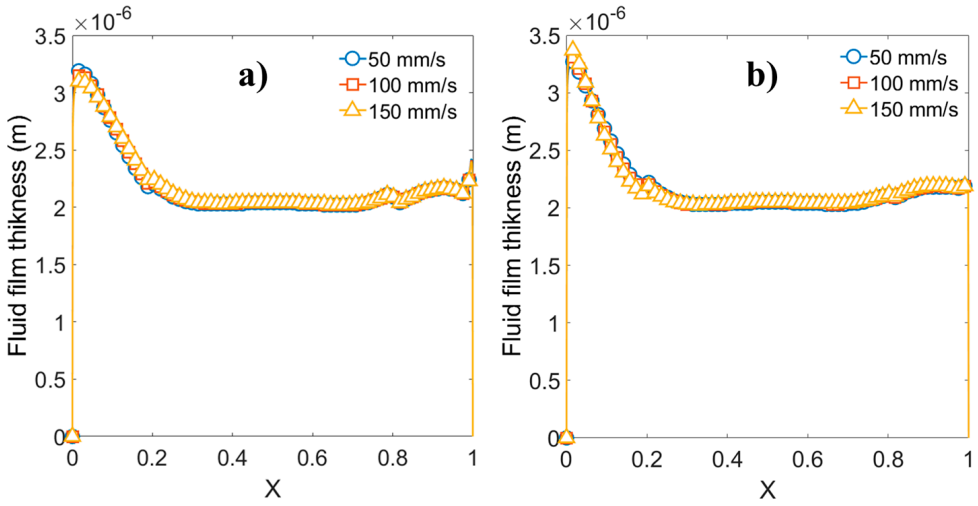


Figure 17. Fluid film thickness at different piston velocities in the instroke (**a**) and outstroke (**b**) directions. Sealed pressure: 5 MPa.

Figure 18 shows the fluid film pressure and the asperity contact pressure distributions with different flow factors (γ), at 5 MPa, 10 MPa, and 15 MPa of sealed pressure, with 100 mm/s of piston velocity in the instroke and outstroke directions. It is observed that transversely oriented asperities ($\gamma = 1/9$) develops a larger fluid film pressure in the first section of the channel compared with the isotropic ($\gamma = 1$) and longitudinally ($\gamma = 9$) oriented, and this behavior is in good agreement with the literature [14]. Furthermore, this observation is more obvious in the case of 5 MPa of sealed pressure, and it becomes less apparent as the sealed pressure increases. However, this difference is only seen near the oil side of the sealing zone (X = 0), until a point at around X = 0.4, after which the pressures converge to a value around zero for the outstroke motion cases. On the other hand, in the instroke motion cases, the fluid film pressure does not present much change with different asperity orientations at the oil side of the sealing zone. Nonetheless, the moderate increase in the fluid film pressure near the air side of the sealing zone, explained before, becomes more apparent with transversely oriented asperities and, similar to the outstroke motion, this increment is more visible in the case of 5 MPa of sealed pressure.

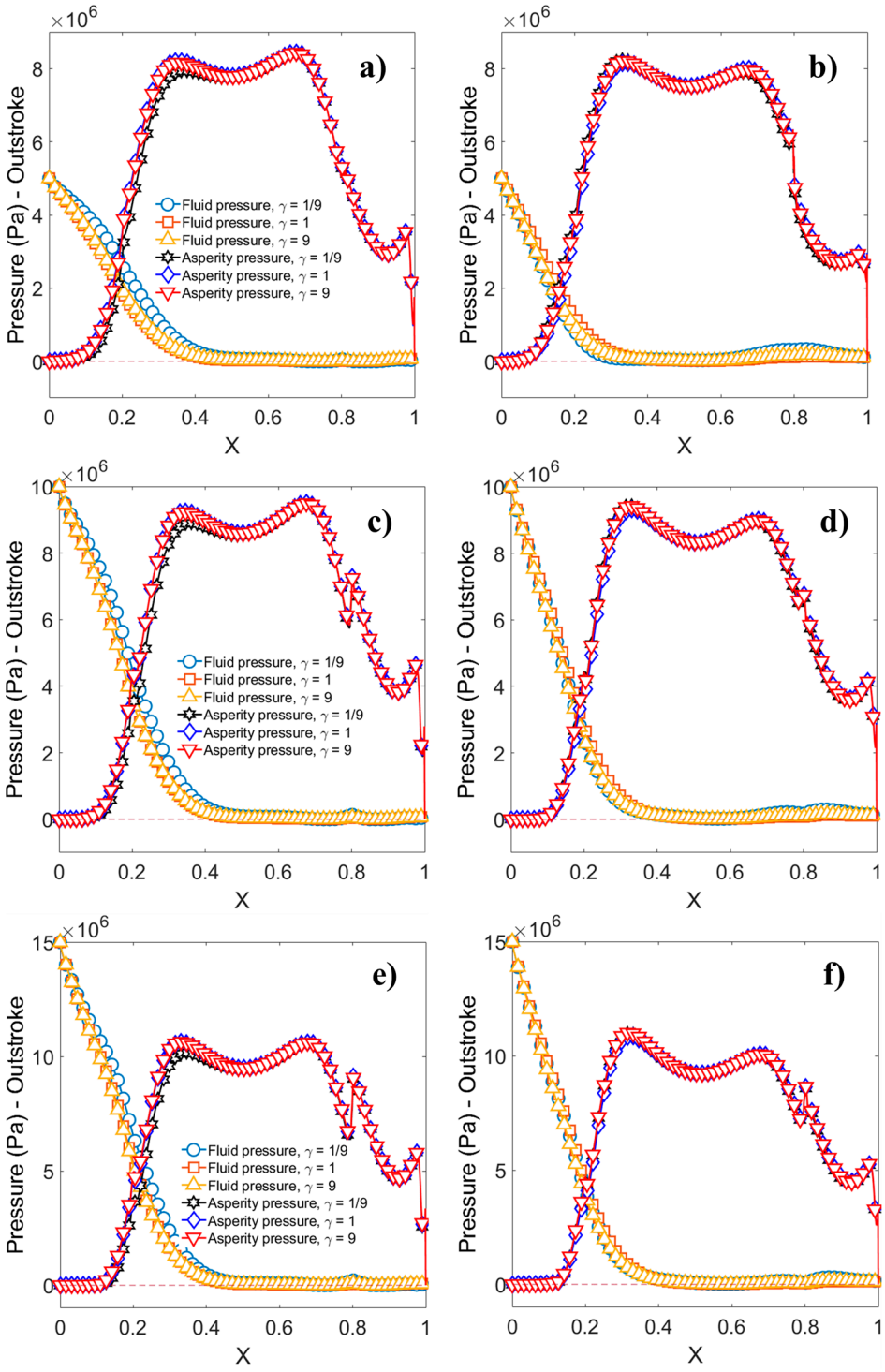


Figure 18. Fluid film and asperity contact pressure distribution with different sealing pressure and flow factors: (**a**,**b**) 5 MPa, (**c**,**d**) 10 MPa, (**e**,**f**) 15 MPa. Piston velocity: 100 mm/s.

In terms of the fluid film thickness, as the surface with transversely oriented asperities starts its reciprocating motion, the fluid carried in the asperity valleys results in an additional flow transport, increasing the mean flow. In contrast, with longitudinally oriented asperities the asperity valleys carries less fluid, which reduces the flow transport. This consequently leads to thicker fluid films when the asperities are transversely oriented in comparison to isotropic and longitudinally oriented asperities, as shown in Figure 19. This difference is only visible near the oil side of the sealing zone, where the fluid film pressure

is substantially bigger than the static contact pressure. Further downstream, the fluid film thicknesses for different asperity orientations converge to similar values.

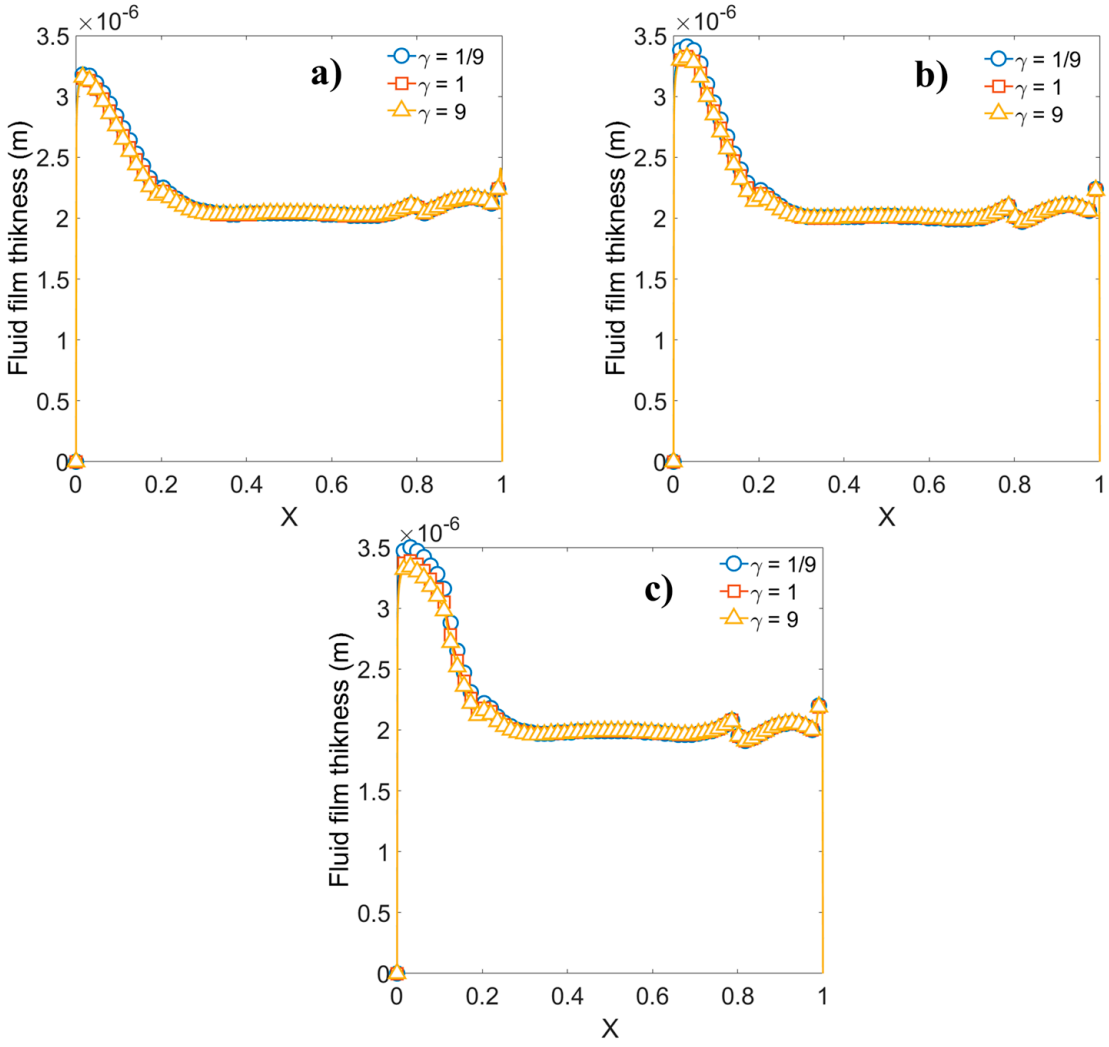


Figure 19. Fluid film thickness distribution for different γ values at 100 mm/s of piston velocity in the outstroke direction for: (**a**) 5 MPa sealed pressure, (**b**) 10 MPa sealed pressure, and (**c**) 15 MPa sealed pressure.

3.3. Friction

The friction force was analyzed with the parameters stated in Table 4. For isotropic asperities, it was found that, in the outstroke and instroke directions (Figures 20 and 21, respectively), the friction force increases linearly with the sealed pressure. This can be explained by Figure 15, where increasing the sealing pressure results in large values of static contact pressure, resulting in large values of asperity contact pressure. As mentioned before, the hydrodynamic effect is weak in most of the sealing zone, which leaves the asperity contact pressure as the primary contributor of the friction force (Coulomb's friction F_c). Furthermore, as observed from Figure 20, a linear decrease in the friction force occurs when the piston velocity increases. This effect can be explained by analyzing Figure 16, where high values of piston velocity produce larger values of fluid film pressure, which in turn reduce the asperity contact pressure.

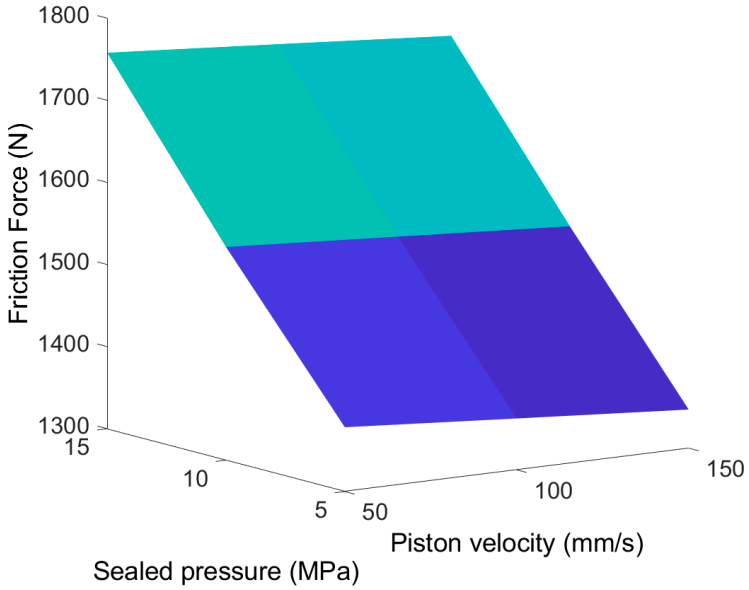


Figure 20. Variation in friction force with sealed pressure and piston velocity in the outstroke direction with isotropic asperities ($\gamma = 1$).

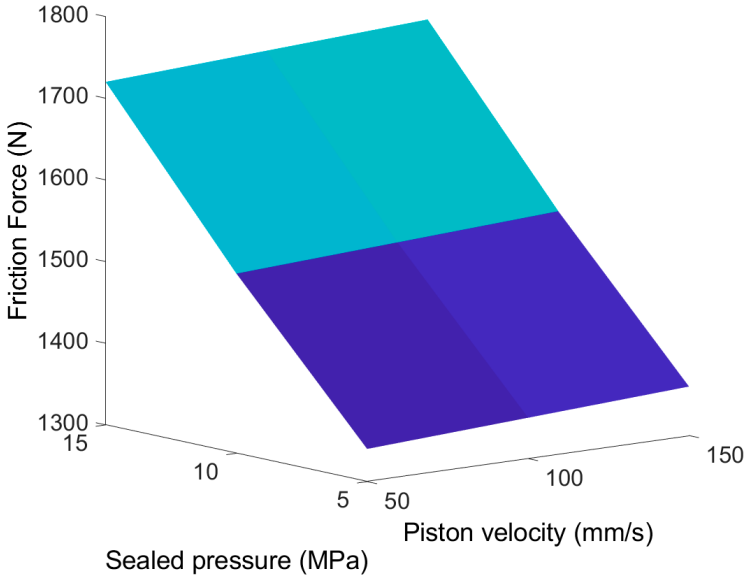


Figure 21. Variation in friction force with sealed pressure and piston velocity in the instroke direction with isotropic asperities ($\gamma = 1$).

Different from the outstroke motion, in Figure 21 a small linear increase in the friction force is noted with higher piston velocities. This can be explained by observing in Figure 16 that, in the instroke motion, increasing the piston velocity only benefits the hydrodynamic effect near the air side (X = 1) in a small portion of the contact zone. Furthermore, in the remainder of the contact zone there is cavitation and, in the contact area near the oil side (X = 0), there is a negative effect in the fluid film pressure as it is reduced. This leads to an increase in the asperity contact pressure (which increase the friction consequently) near the oil side of the channel before reaching cavitation at a point around X = 0.4.

Figure 22 presents the friction force for different asperity orientations and sealed pressures. In the case of the outstroke motion, the friction force is smaller when the asperities are transversely oriented than when they are longitudinally oriented. This observation is consistent for all the sealed pressures investigated in this paper. This can be attributed to the enhanced hydrodynamic effect observed in the contact zone near the

oil side (X = 0) with transversely oriented asperities, as shown in Figure 18. In turn, this effect decreases the asperity contact pressure in the aforementioned contact zone. Another physical explanation is that, as the flow with transversely oriented asperities starts its reciprocating motion, the fluid carried in the asperity valleys results in an additional flow transport, increasing the mean flow and the film thickness (in near proximity to the oil side of the contact zone), as shown in Figure 19. Different from the outstroke motion, the orientation of the asperities has almost negligible effect on the friction force in the instroke direction. This can be explained from the results presented in Figure 18, as there is close to zero effect on the fluid film pressure with the change in asperity orientations. This means that, on average for all the asperity orientation cases, the static contact pressure remains relatively unchanged, thus not having any significant effect on the friction force.

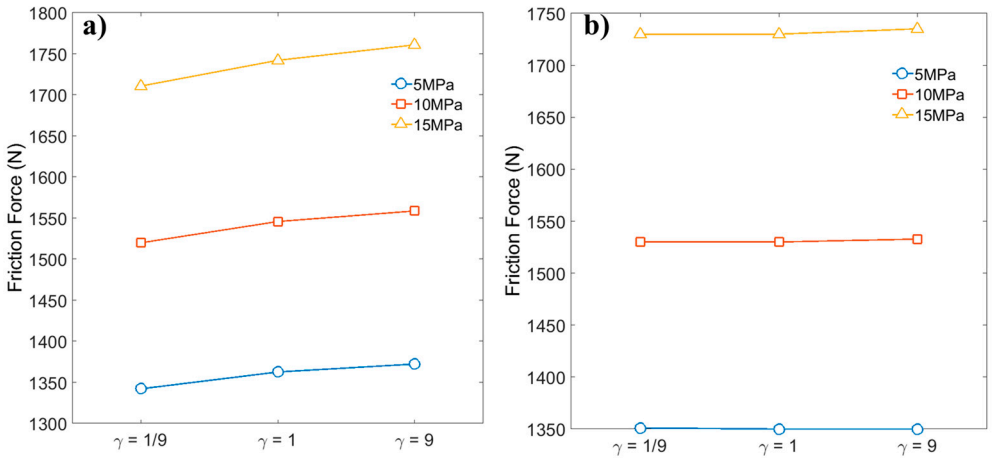


Figure 22. Friction force for different asperity orientations and sealed pressures. Piston velocity of 100 mm/s in the (**a**) outstroke and (**b**) instroke directions.

Figure 23 display the friction force components for the case of 100 mm/s of piston velocity with isotropic asperities. It is not difficult to see that the asperity friction contributes almost entirely to the total friction force, at 99.75% of the friction in the case of 15 MPa of sealed pressure. This is expected because, in most of the sealing zone, the asperity contact pressure is substantially larger than the fluid film pressure, resulting in fluid films thin enough for asperity contact to take place. Thus, the hydrodynamic effect is weak in most areas of the contact zone for all the sealed pressures, piston velocities, and asperity orientation cases.

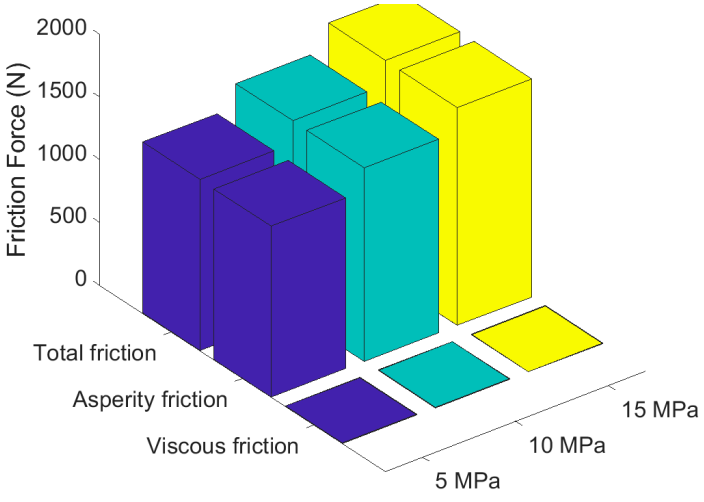


Figure 23. Friction force components at 5 MPa of sealed pressure and different piston velocities. Isotropic asperities.

3.4. Deformation Verification

The fluid film thickness is iteratively adjusted by adding the elastic deformation model defined in Equation (16) until the convergence criteria of a minimum P_{def} is reached, as shown in Figure 7. It is important to verify the deformation calculated with this model, due to the substantial influence that the fluid film thickness has in the fluid film and asperity pressure distributions, friction, and leakage. To do this, the pressure balance P_{def} distribution in the contact zone at the last iteration was applied to the FEM model as a pressure boundary condition in the nodes enclosed by the contact area (backup rings and cap). It can be seen from Figure 24 that, apart from some spikes in a few nodes from the FEM, the general trend in the deformation estimated by the model applied in this work (Δh from Equation (16)) is in good agreement with the nodal deformation obtained by the FEM.

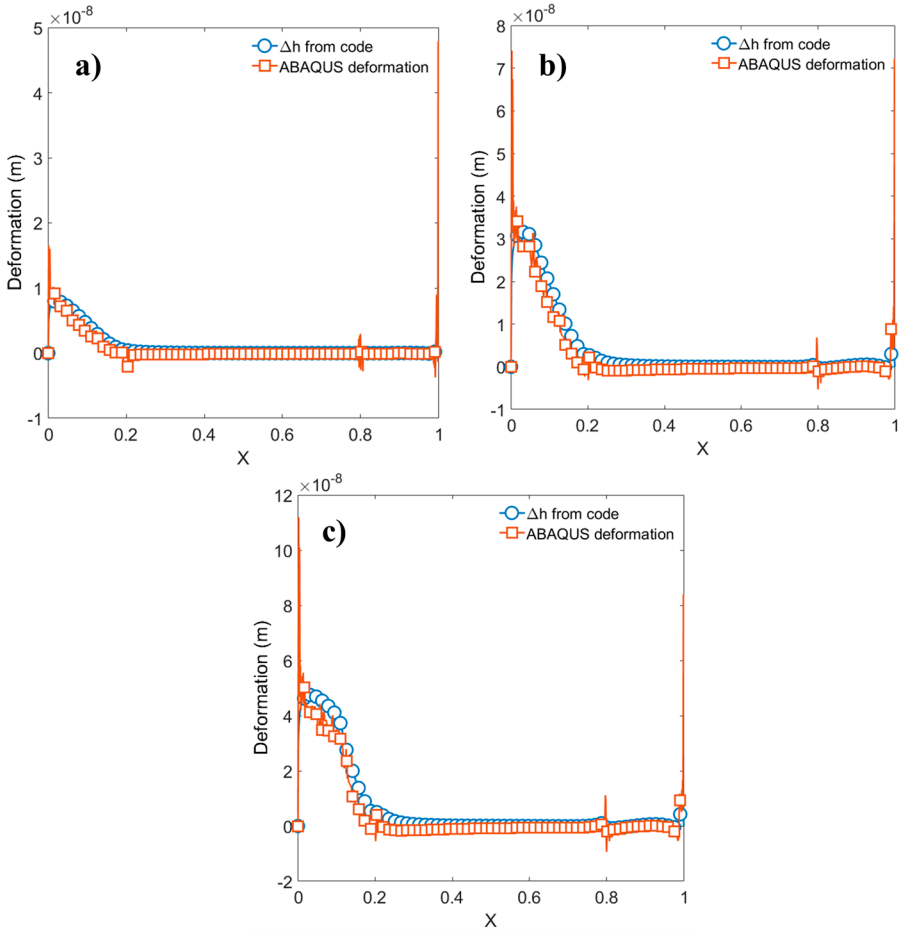


Figure 24. Elastic deformation comparison: (**a**) 5 MPa of sealed pressure, (**b**) 10 MPa of sealed pressure, (**c**) 15 MPa of sealed pressure.

3.5. Oil Leakage Calculation

The flow rate per unit circumferential length (q from Equation (20)) was studied with the parameters stated in Table 4. Figure 25 presents the flow rate calculated from Equation (20) at different sealed pressures in the instroke and outstroke directions along the sealing zone, with isotropic asperities and a piston velocity of 100 mm/s. The negative flow rates correspond to the instroke flow direction and the positives flow rates correspond to the outstroke flow direction. From the figure, it is noted that the sealed pressure has a strong influence on the flow rate for this range of pressures. Increasing the sealing pressure increases the value of the flow rate in the instroke and outstroke motions, being relatively constant in most of the contact zone. It is found that the flow rate is linear in the sealing

zone, where the slope $\frac{\partial(F\Phi)}{\partial X} = 0$. This behaviour agrees with the literature for simpler O-ring applications [13].

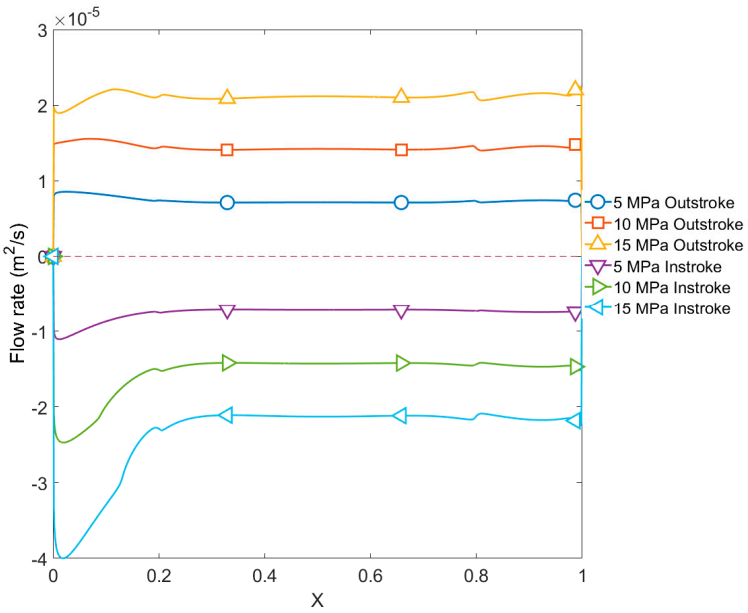


Figure 25. Flow rate per unit circumferential length at different sealed pressures in the instroke and outstroke motion. Isotropic asperities and piston velocity of 100 mm/s.

Similarly to the sealing pressure, the piston velocity also influences the flow rates. Figure 26 shows q at different piston velocities in the instroke and outstroke motion; the sealed pressure is 10 MPa with isotropic asperities along the contact zone. As the speed is increased, the magnitude of q increases, which is expected, as the flow rate is proportional to the piston speed. Another parameter that has an impact on the flow rates is the direction of the asperities, as portrayed in Figure 27.

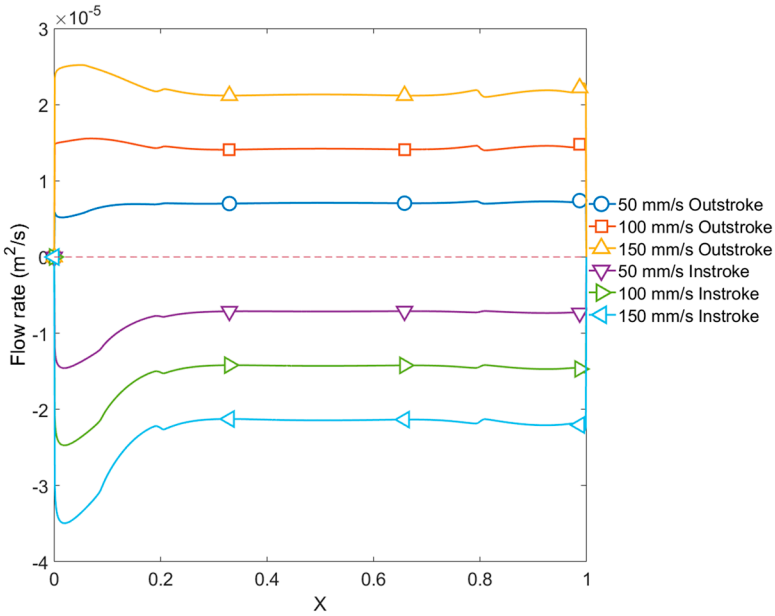


Figure 26. Flow rate per unit circumferential length at different piston velocities in the instroke and outstroke motion. Isotropic asperities and sealed pressure of 10 MPa.

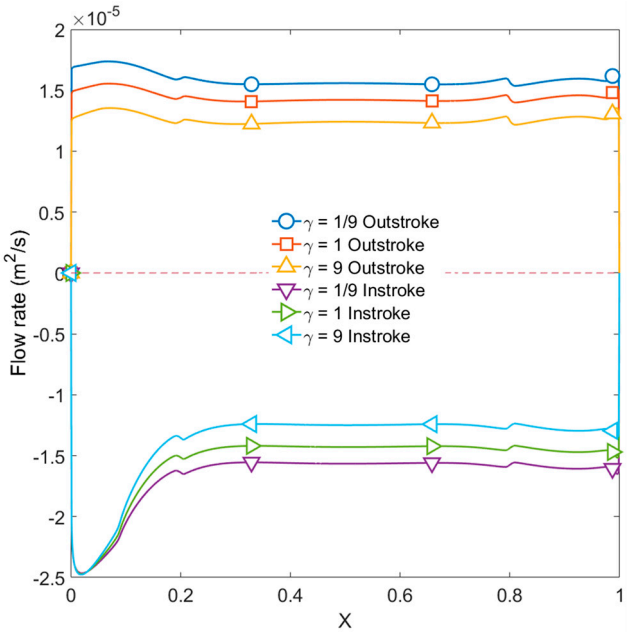


Figure 27. Flow rate per unit circumferential length at different asperity orientation in the instroke and outstroke motion. Piston velocity of 100 mm/s and sealed pressure of 10 MPa.

Transversely oriented asperities ($\gamma = 1/9$) promote larger values of q, which means that transversely oriented asperities not only generate additional flow transport (see Figure 19), increasing the fluid film thickness, but also drive the flow rate to higher values. It is not difficult to see that the change in q due to the change in the asperity's orientation is not as substantial as the cases when piston velocity and sealed pressure are varied. For instance, increasing the piston velocity from 100 mm/s to 150 mm/s corresponds to an increase by 33% in the average q, for the case of 10 MPa of sealed pressure and isotropic asperities. On the other hand, changing the asperities from isotropic ($\gamma = 1$) to transversely oriented ($\gamma = 1/9$), with a piston velocity of 100 mm/s and 10 MPa of sealed pressure, only increases the average flow rate by 10%, highlighting the influence that each input parameter from Table 4 has on the fluid flow rate and, subsequently, the flow volume.

The oil leakage can be expressed as the amount of flow volume obtained from Equation (21), exiting the contact zone in a full stroke on a piston with 0.359 m of circumference and a stroke length of 0.2 m. These dimensions were chosen based on an example of a generic landing gear shock absorber in small aircraft from [2]. The average flow volume in the outstroke and instroke motion is presented in Figure 28 for the different input parameters chosen for this study. The positive flow volume correspond to the fluid flow in the outstroke direction moving towards the air side of the sealing zone (out-leakage), and the negative flow volume to the instroke direction moving towards the oil side of the contact zone (in-leakage). A correlation between the volumetric flow in the outstroke and instroke motion and the input parameters from Table 4 is found. Increasing the sealed pressure and the piston velocity is followed by an increase in volume flow in both instroke and outstroke directions. The flow volume is further enlarged when the asperities are transversely oriented ($\gamma = 1/9$). However, it is noted that the influence of the asperity orientation on the flow volume grows with piston velocity and sealed pressure. For instance, when the sealed pressure is 15 MPa and the piston velocity 150 mm/s, changing the γ value seems to have a more considerable effect than when the sealed pressure is 5 MPa and 50 mm/s, where the asperity orientation plays a negligible part. However, in all cases, transversely oriented asperities present more flow volume than the isotropic and longitudinally oriented, with the latter yielding minimum flow volume.

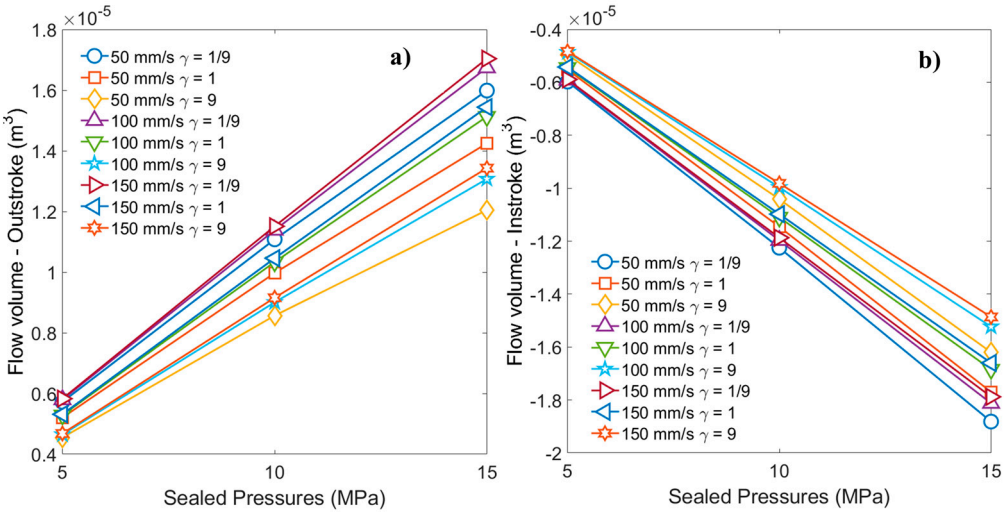


Figure 28. Flow volume in the (**a**) outstroke and (**b**) instroke motion.

The net oil flow volume or leakage in a full stroke is defined as the difference between the volumetric flow in the outstroke and instroke directions. Figure 29 presents the net oil leakage in a full stroke with a stroke length of 0.2 m and a piston circumference of 0.359 m, calculated where the slope $\frac{\partial(F\Phi)}{\partial X} = 0$. From the figure, it is noted that, in all cases, the net oil leakage is negative, which means that there is inflow of oil into the sealed space or oil chamber in all the input parameters defined in Table 4. Thus, for this set of working and boundary conditions, out-leakage is not expected. This is in good agreement with previous literature on O-ring seals, Thatte et al. [22] reported that thinner films during the outstroke motion and cavitation, mainly during the outstroke, are characteristics of non-leaking seals.

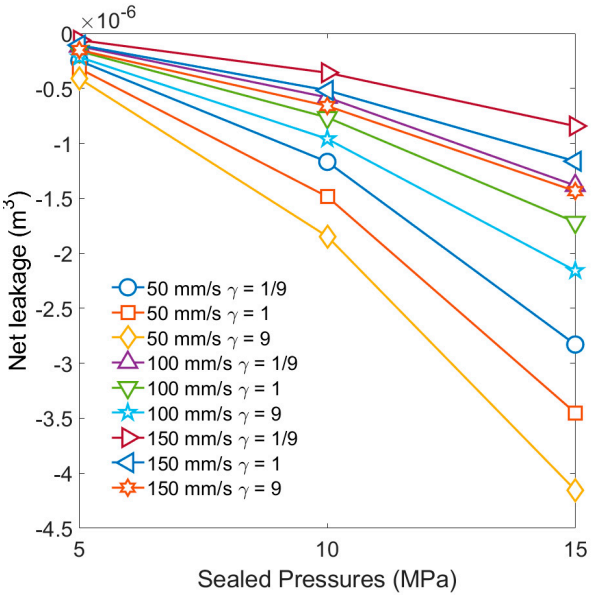


Figure 29. Net flow volume.

Results from Figure 28 highlight the importance of the asperity orientation in computationally estimating the leakage, especially at high sealed pressures. It is clear that, for the case of 5 MPa, the orientation of the asperities does not influence considerably the volume flow. However, when the sealed pressure is increased, the effect of the asperities become more significant, which begs the question as to their role when calculating leakage in sealing systems. It is not surprising that asperity orientation is included in recent computational

EHL research, such as that of Kumar et al. [14] and Masjedi et al. [16]. However, it is not common practice to vary these parameters for computational seal leakage studies.

4. Conclusions

This study presents a computational model that describes the fluid film pressure distribution, the asperity contact pressure, and the fluid film thickness deformation in the sealing area of a reciprocating multi-material CTR seal at different sealing pressures and piston speeds, as well as asperity orientations. In this work, the fluid film was divided in three sections with different elastic properties, thus affecting the fluid film deformation from one section to another. The FEM used to obtain static contact pressure, which is essential to calculate the flow properties, such as fluid pressure and film thickness in the sealing area, is also described.

A linear elastic deformation model was used in a multi-material contact zone, with different mechanical properties in each section of the fluid channel. The film deformation was verified with results from FEM, using the pressure balance P_{def} as a pressure boundary condition. This suggest that the elastic deformation model chosen is suitable for this problem, as the deformation estimated by the model applied in this work was in good agreement with the nodal deformation obtained by the FEM.

It was found that the fluid film pressure increases with the piston speed in the outstroke direction. At piston speed of 150 mm/s, the fluid film pressure along the channel is larger than at 100 mm/s and decreases further at 50 mm/s. This behavior agrees with earlier investigations of simple seals [19]. In addition, it was established that, differently from simple O-ring studies [19], where in the instroke condition the fluid pressure decrease without reaching cavitation, in the CTR seal the fluid film pressure decreases continuously until the middle of the sealing area, where it reaches cavitation. Subsequently, the pressure increases near the air side, which is more pronounced with higher piston speeds. This phenomenon is similar to the behavior of slip ring combination seals [23].

Furthermore, the present numerical simulations show that, as the fluid film pressure decreases along the sealing zone reaching cavitation conditions, the asperity contact pressure increases as the fluid film thickness shrinks because of the static contact pressure peaks obtained from the FEM, following the balance equation (Equation (16)).

During this research it was established that transversely oriented asperities generate higher fluid film pressure distributions and thicker fluid film thickness. In contrast, longitudinally oriented asperities promote smaller fluid film pressure distributions. Hence, conclusions from earlier numerical studies [14,16] were verified. Analyzing the effect of the asperity orientation in the flow rate per unit circumferential length, a general trend of a reduced flow rate as the asperities becomes longitudinally oriented was found, which means transversely oriented asperities would produce more leakage than longitudinally oriented. However, a tendency to reduce the friction force was found when the asperities are transversely oriented to the fluid flow, as they promote thicker fluid films. Thus, reducing the leakage by minimizing the film thickness when asperities are longitudinal involves higher values of friction as a trade-off for this set of boundary conditions and input parameters.

Furthermore, the volumetric flow was found to increase with the sealed pressure and piston velocity in both instroke and outstroke directions. However, for this set of boundary conditions and input parameters out-leakage is not expected.

Parameters not varying in this study include those related to novel hyper-elastic materials and new types of lubricant oils. Limitations of the model include variation in the temperature, which could be introduced by estimating its effect on the oil viscosity in a thermal EHL model [31]. The static contact pressure distribution is not only associated with the sealing pressure, but is also influenced by the geometry configuration of the sealing system (rubber seal shape, backup rings, and cap). The effect of the geometry configuration of the sealing system on the static contact pressure and the sealing performance warrants further investigation, made possible by the herein presented computational framework.

Author Contributions: A.F.A. (Aaron Feria Alanis): Principal author, writing and editing, data generation analysis, and figures generation. A.A.S.A.-S.: Data analysis, rewriting, and supervision. A.F.A. (Antonis F. Antoniadis): Conceptualization, funding acquisition, and data analysis. P.T.: Supervision and data analysis. M.S.: Conceptualization, funding acquisition, rewriting, and supervision. All authors have read and agreed to the published version of the manuscript.

Funding: This work was conducted under the ATI/Innovate UK (Grant No. 263261) Project: Future Landing Gear 2, with Airbus UK as Industrial Lead. The authors also acknowledge funding from EPSRC (Grant No. 2625870).

Data Availability Statement: The data presented in this study are openly available at: https://doi.org/10.57996/cran.ceres-2666, accessed on 12 November 2024.

Conflicts of Interest: The authors declare that there are no conflicts of interest regarding the publication of this paper.

Nomenclature

c	Circumference of the piston
CTR	Capped T-ring
CR	Compression ratio
C_{10}, C_{01}	Mooney–Rivlin constants
E	Elastic modulus
f_c	Friction coefficient
H	Dimensionless film thickness
h	Fluid film thickness
Δh	Fluid film deformation
H_T	The dimensionless average film thickness
HA	Shore A hardness
I_1, I_2	Strain tensors invariants
L	Length of the stroke
P	Dimensionless fluid pressure
$P_{c_{dim}}$	Asperity contact pressure
P_a	Sealed pressure
P_{atm}	Ambient pressure
P_c	Dimensionless asperity contact pressure
P_{def}	Pressure balance
P_f	Fluid pressure
P_{sc}	Static contact pressure
q	Flow rate per unit circumferential length
Q	Flow volume on a full stroke
$\hat{q}$	Dimensionless flow rate
$\overline{Q}$	Net flow volume
$\overline{q}_{xa}$	Mean flow transport
q_{ins}	Instroke flow rate
q_{out}	Outstroke flow rate
R	Asperity radius
U	Piston speed
W	Strain energy density
X	Dimensionless x-coordinate
x	x-coordinate
x_l	Length of channel
X_L	Dimensionless length of channel
α	Viscosity-pressure coefficient
γ	Asperity orientation parameter
η_0	Fluid viscosity at atmospheric pressure

$\lambda_{0.5x}$, $\lambda_{0.5y}$	Asperity lengths
λ_j	Principal stretch components
ν	Poisson's ratio
ξ	Dimensionless piston speed constant
ρ	Asperity density
$\hat{\rho}$	Dimensionless fluid density
σ	Root mean squared (RMS) roughness
$\hat{\sigma}$	Dimensionless RMS roughness
Φ_{scx}	Shear flow factor
Φ_{xx}	Pressure flow factor

References

1. Nikas, G.K. Eighty years of research on hydraulic reciprocating seals: Review of tribological studies and related topics since the 1930s. *Proc. Inst. Mech. Eng. Part J J. Eng. Tribol.* **2010**, *224*, 1–23. [CrossRef]
2. Currey, N.S. *Aircraft Landing Gear Design: Principles and Practices*; AIAA Education Series: Reston, VA, USA, 1988.
3. Flitney, R. *Seals and Sealing Handbook*; Elsevier Ltd.: Amsterdam, The Netherlands, 2014.
4. Karaszkiewicz, A. Geometry and contact pressure of an O-ring mounted in a seal groove. *Ind. Eng. Chem. Res.* **1990**, *29*, 2134–2137. [CrossRef]
5. Zhang, J.; Xie, J. Investigation of Static and Dynamic Seal Performances of a Rubber O-Ring. *J. Tribol.* **2018**, *140*, 042202. [CrossRef]
6. Sukumar, T.; Bapu, B.R.; Prasad, B.D. Prediction of hyperelastic material sealing pressure using experimental and numerical analyses. *J. Elastomers Plast.* **2020**, *52*, 717–727. [CrossRef]
7. Zhang, S.; Deng, S.; Zhang, W.; Kang, N. Simulation and experiment on sealing mechanism with rigid-flexible combined seal groove in hub bearing. *Tribol. Int.* **2019**, *136*, 385–394. [CrossRef]
8. Zhou, C.; Chen, G.; Liu, P. Finite Element Analysis of Sealing Performance of Rubber D-Ring Seal in High-Pressure Hydrogen Storage Vessel. *J. Fail. Anal. Prev.* **2018**, *18*, 846–855. [CrossRef]
9. Zhou, C.; Zheng, J.; Gu, C.; Zhao, Y.; Liu, P. Sealing performance analysis of rubber O-ring in high-pressure gaseous hydrogen based on finite element method. *Int. J. Hydrogen Energy* **2017**, *42*, 11996–12004. [CrossRef]
10. Zhang, H.; Zhang, J. Static and Dynamic Sealing Performance Analysis of Rubber D-Ring Based on FEM. *J. Fail. Anal. Prev.* **2016**, *16*, 165–172. [CrossRef]
11. Tsala, S.; Berthier, Y.; Mollon, G.; Bertinotti, A. Numerical Analysis of the Contact Pressure in a Quasi-Static Elastomeric Reciprocating Sealing System. *J. Tribol.* **2018**, *140*, 064502. [CrossRef]
12. Hess, D.P.; Soom, A. Friction at a Lubricated Line Contact Operating at Oscillating Sliding Velocities. *J. Tribol.* **1990**, *112*, 147–152. [CrossRef]
13. Karaszkiewicz, A. Hydrodynamic lubrication of rubber seals for reciprocating motion; leakage of seals with an O-ring. *Tribol. Int.* **1988**, *21*, 361–367. [CrossRef]
14. Kumar, R.; Azam, M.S. Effect of directionally oriented random roughness on performance of a Rayleigh step bearing operating under Mixed-Elastohydrodynamic Lubrication. *Tribol. Int.* **2021**, *153*, 106572. [CrossRef]
15. Pei, J.; Han, X.; Tao, Y.; Feng, S. Mixed elastohydrodynamic lubrication analysis of line contact with Non-Gaussian surface roughness. *Tribol. Int.* **2020**, *151*, 106449. [CrossRef]
16. Masjedi, M.; Khonsari, M. Mixed elastohydrodynamic lubrication line-contact formulas with different surface patterns. *Proc. Inst. Mech. Eng. Part J J. Eng. Tribol.* **2014**, *228*, 849–859. [CrossRef]
17. Prati, E.; Strozzi, A. A Study of the Elastohydrodynamic Problem in Rectangular Elastomeric Seals. *J. Tribol.* **1984**, *106*, 505–512. [CrossRef]
18. Stupkiewicz, S.; Marciniszyn, A. Elastohydrodynamic lubrication and finite configuration changes in reciprocating elasto-meric seals. *Tribol. Int.* **2009**, *42*, 615–627. [CrossRef]
19. Yuan, X.; Wang, J.; Lian, Z.; Wang, G. Partial lubrication modeling of reciprocating rod seals based on a developed EHL method. *Tribol. Int.* **2021**, *153*, 106585. [CrossRef]
20. Han, Q.; Chen, H.; Yang, W.; Zhang, Y.; Yang, J.; Chen, Y. Analysis of reciprocating O-ring seal in the pressure-balanced oil-filled wet-mate electrical connectors for underwater applications. *Lubr. Sci.* **2019**, *31*, 335–345. [CrossRef]
21. Greenwood, J.A.; Williamson, J.B.P. Contact of nominally flat surfaces. *Proc. R. Soc. London. Ser. A. Math. Phys. Sci.* **1966**, *295*, 300–319. [CrossRef]
22. Thatte, A.; Salant, R.F. Transient EHL analysis of an elastomeric hydraulic seal. *Tribol. Int.* **2009**, *42*, 1424–1432. [CrossRef]
23. Zhang, Y.; Lou, Z.; Wei, F.; Lin, S.; Hu, L.; He, W. Hybrid lubrication model study of slip ring combination seal under the influence of frictional heat. *Proc. Inst. Mech. Eng. Part J J. Eng. Tribol.* **2024**, *238*, 426–449. [CrossRef]
24. Mooney, M. A Theory of Large Elastic Deformation. *J. Appl. Phys.* **1940**, *11*, 582–592. [CrossRef]
25. Rivlin, R.S. Large elastic deformations of isotropic materials IV. further developments of the general theory. *Philos. Trans. R. Soc. London. Ser. A Math. Phys. Sci.* **1948**, *241*, 379–397. [CrossRef]

26. Patir, N.; Cheng, H.S. Application of Average Flow Model to Lubrication Between Rough Sliding Surfaces. *J. Lubr. Technol.* **1979**, *101*, 220–229. [CrossRef]
27. Patir, N.; Cheng, H.S. An Average Flow Model for Determining Effects of Three-Dimensional Roughness on Partial Hydrodynamic Lubrication. *J. Lubr. Technol.* **1978**, *100*, 12–17. [CrossRef]
28. Timoshenko, S.; Goodier, J.N. *Theory of Elasticity*; McGraw-Hill Book Company, Inc.: Chicago, IL, USA, 1951.
29. Peng, C.; Ouyang, X.; Zhu, Y.; Guo, S.; Zhou, Q.; Yang, H. Investigation into the influence of stretching on reciprocating rod seals based on a novel 3-D model vs axisymmetric model. *Tribol. Int.* **2018**, *117*, 1–14. [CrossRef]
30. Zhou, G.; Zhang, Y.; Wang, Z.; Pu, W. Analysis of transient mixed elastohydrodynamic lubrication in planetary roller screw mechanism. *Tribol. Int.* **2021**, *163*, 107158. [CrossRef]
31. Ardah, S.; Profito, F.J.; Dini, D. An integrated finite volume framework for thermal elasto-hydrodynamic lubrication. *Tribol. Int.* **2023**, *177*, 107935. [CrossRef]

Disclaimer/Publisher's Note: The statements, opinions and data contained in all publications are solely those of the individual author(s) and contributor(s) and not of MDPI and/or the editor(s). MDPI and/or the editor(s) disclaim responsibility for any injury to people or property resulting from any ideas, methods, instructions or products referred to in the content.



https://dspace.org/

A mixed-elastohydrodynamic lubrication model of a capped-T-ring seal with a sectioned multi-material film thickness in landing gear shock absorber applications

Feria Alanis, Aaron; Sheikh Al-Shabab, Ahmed A.; Antoniadis, Antonis F.; Tsoutsanis, Panagiotis; Skote, Martin

2024-12-01
MDPI
https://doi.org/10.3390/fluids9120271
Feria Alanis A, Sheikh Al-Shabab AA, Antoniadis AF, et al., (2024) A mixed-elastohydrodynamic lubrication model of a capped-T-ring seal with a sectioned multi-material film thickness in landing gear shock absorber applications. Fluids, Volume 9, Issue 12, December 2024, Article number 271

Downloaded from a DSpace repository. https://dspace.org/